

Novel Source-Sink Model for Space Environment Evolution with Orbit Capacity Assessment

Andrea D'Ambrosio, * Simone Servadio, † Peng Mun Siew, † and Richard Linares † Massachusetts Institute of Technology, Cambridge, Massachusetts 02139

https://doi.org/10.2514/1.A35579

The increasing number of anthropogenic space objects (ASOs) in low Earth orbit (LEO) poses a threat to the safety and sustainability of the space environment. Multiple companies are planning to launch large constellations of hundreds to thousands of satellites in the near future, increasing the probability of collisions and debris generation. This paper analyzes the long-term evolution of the LEO ASO population with the goal of estimating LEO orbital capacity. This is carried out by introducing a new probabilistic source-sink model. The developed source-sink model is a multishell multispecies model, which includes different object species, such as active and derelict satellites, and debris. Furthermore, debris are divided into the following two subgroups: trackable and nontrackable debris, the last ones representing a significant hazard for active satellites. In addition, the proposed model accounts for collision events and atmospheric drag effects, which include the influence of solar activity. Indeed, the Jacchia-Bowman 2008 thermospheric density model is exploited. The results prove that considering untracked debris within the model produces more collisions, and therefore a smaller population of active satellites affecting the safety of LEO and its orbital capacity.

| Nomenclature | | | | |
|---------------------|---|--|--|--|
| \boldsymbol{A} | = | area of an object, m ² | | |
| B | = | 1 11 | | |
| B_n | = | bandwidth, 1/s | | |
| b | = | object diameter, m | | |
| Ċ | = | number of objects removed/added per year due to a collision | | |
| $\dot{C}_{ m add}$ | = | gain in derelicts and debris per year due to a collision | | |
| c_D | = | drag coefficient | | |
| D | = | derelict | | |
| d | = | thickness of shell, km | | |
| \dot{F} | = | flux due to atmospheric drag, objects/year | | |
| F_{max} | = | maximum value of solar flux | | |
| F_{mean} | = | mean value of solar flux | | |
| F_{min} | = | minimum value of solar flux | | |
| $G_{t/r/p}$ | = | transmitter/receiver/signal processing gains, dB | | |
| h | = | altitude of shell, km | | |
| K_{ij} | = | matrix containing number of fragments generated from a collision | | |
| k | = | Boltzmann constant, $m^2 \cdot kg \cdot s^{-2} \cdot K^{-1}$ | | |
| L_C | = | characteristic length, m | | |
| $L_{P/S}$ | = | propagation/system loss, dB | | |
| M | = | mass of objects involved in a catastrophic collision, kg | | |
| M_p | = | mass of projectile in a noncatastrophic collision, kg | | |
| m | = | mass of a generic object, kg | | |
| N | = | trackable debris | | |
| N_s | = | number of species considered | | |
| $P_{\rm det}$ | = | probability of detection | | |
| P_{fa} | = | probability of false alarm | | |
| P_{M} | = | probability of success of postmission disposal | | |

Presented as Paper 2022-658 at the 2022 AAS/AIAA Astrodynamics Specialist Conference, Charlotte, NC, August 7-11, 2022; received 4 October 2022; revision received 26 December 2022; accepted for publication 8 January 2023; published online 31 January 2023. Copyright © 2023 by the American Institute of Aeronautics and Astronautics, Inc. All rights reserved. All requests for copying and permission to reprint should be submitted to CCC at www.copyright.com; employ the eISSN 1533-6794 to initiate your request. See also AIAA Rights and Permissions www.aiaa.org/randp.

*Postdoctoral Associate, Department of Aeronautics and Astronautics, 77 Massachusetts Avenue; andreada@mit.edu. [†]Postdoctoral Associate, Department of Aeronautics and Astronautics, 77

*Rockwell International Career Development Professor, Associate Profes-

sor of Aeronautics and Astronautics, Department of Aeronautics and Astronautics, 77 Massachusetts Avenue. Senior Member AIAA.

| P_t | = | peak power, W |
|----------|---|-----------------|
| α | _ | generic species |

radar-object distance, km distance from center of Earth, km radius of an object, m

S active satellite

 T_S T_0 Usystem noise temperature, K noise temperature, K untrackable debris

V(h)volume of orbital shell, km³ change in semimajor axis, km/s

 v_c orbital speed at average population altitude, km/s $v_{
m imp}$ impact velocity in a noncatastrophic collision, km/s

 $v_r(h)$ average relative velocity, km/s dimensionless diameter х

dimensionless radar cross section

fractions of collisions that an active satellite fails to α avoid (only with derelicts and tracked debris)

fractions of collisions that an active satellite fails to α_a

avoid (only among active satellites)

fractions of collisions that an active satellite fails to $\alpha_{\rm su}$ avoid (only with untracked debris)

Γ matrix of coefficients

loss of custody of tracked debris γ_n

fraction related to γ_n $\gamma_{n,\%}$

 Δt satellite operation life, years

δ ratio of density of disabling to lethal trackable debris δ_{su} ratio of density of disabling to lethal untrackable debris fraction of successful tracking of untracked debris

 η_n fraction related to η_n $\eta_{n,\%}$

λ annual launch rate, objects/year

 λ_w signal wavelength, m

Earth gravitational parameter, km³/s²

ξ ratio of untracked debris generated from a collision

fraction related to ξ atmospheric density, kg/m³ σ_{ij} impact parameter, m² radar cross section

 $\sigma_{
m RCS}$ transmitted pulse width, s

intrinsic probability of collision matrix, 1/year

Subscripts

ccatastrophic collision i, jspecies of a model

noncatastrophic (damaging) collision nc

I. Introduction

R ECENTLY, many companies have planned to launch large satellite constellations with hundreds or thousands of satellites, especially in low Earth orbit (LEO). Among them, there are the SpaceX Starlink constellation, with 4408 currently authorized satellites and a potential final number of about 42,000 satellites [1]; the Amazon Kuiper constellation, with about 3236 satellites authorized and a final number of about 7800 satellites [2]; and Astra Space constellation of about 13,000 satellites [3]. This high number of satellites will lead to an anticipated growth in the LEO anthropogenic space object (ASO) population. Consequently, the higher number of collisions and the corresponding debris creation will produce a significant environmental impact, causing LEO to be a more complex environment to operate. Understanding the evolution of the space environment and the sensitivity of that evolution to different variables is essential to ensure long-term sustainability and to inform work by operators to ensure kinetic space safety. Indeed, new constellations require reliable collision avoidance control, such as satellite slotting, and postmission disposal (PMD) procedures, to minimize the number of new derelicts created.

The current paper investigates the evolution of the ASO population in LEO by exploiting a new probabilistic source-sink model with the objective of estimating the LEO orbital capacity. This is carried out through the long-term propagation of the proposed source-sink model, which is part of the so-called Massachusetts Institute of Technology Orbital Capacity Assessment Tool (MOCAT), which globally considers different object species, such as active satellites, derelict satellites, and debris. In this new model, the debris species are divided into the following two subgroups: trackable and nontrackable debris (also referred to as untracked debris), the last ones representing a significant threat to active satellites. Indeed, the inability to track some debris leads to more unexpected catastrophic events (i.e., collisions) because active satellites cannot perform collision avoidance maneuvers in time. In addition, solar activity and geomagnetic storms, which affect the natural decay of objects through the atmospheric drag flux, are included within the proposed model. This is carried out by employing the Jacchia-Bowman 2008 (JB2008) thermospheric density model [4]. Once introduced, the model will be propagated for long-term predictions of ASO evolution. Subsequently, an estimation of the LEO orbital capacity is provided according to standard metrics.

The orbital capacity can be defined according to the following two approaches: intrinsic capacity of slotted spacecraft and riskbased capacity [5]. Intrinsic capacity correlates the orbital capacity to the number and configuration of active ASOs that can be placed in a region of space to avoid collisions with other active ASOs. On the other hand, risk-based capacity relies on estimating ASO evolution and distribution over time [5]. Even though there is not a commonly accepted metric to measure risk-based capacity, some metrics have been introduced in the literature, such as the numbertime (NT) product [6], associated with the trend of the number of fragments; the Criticality of Spacecraft Index (CSI) [7], which is an analytical index measuring the threat of large intact objects to the environment in terms of possible debris cloud generated in case of fragmentation; and the indices based on the Environmental Consequences of Orbital Breakups index [8] reported in Refs. [9,10]. In particular, these two works also consider some trackability measures within their indices to assess its effect on collision probability, with the result of shifting the most critical regions to higher altitudes. The evolution of ASOs in a specific time frame is usually required to compute the risk-based capacity. In particular, two methodologies can be identified to estimate the evolution of ASOs. The first method exploits a deterministic approach based on the propagation of the ASOs forward in time according to reasonably accurate physical models of spacecraft dynamics. Generally, to reduce computational efforts, semi-analytic propagation techniques are employed for long propagation times. Many perturbations (oblateness of Earth, third-body perturbations, atmospheric drag, solar radiation pressure, and space weather) are modeled as well as collisions and explosions. The advantage of this approach is the exact information that can be obtained about each single ASO. Moreover, this methodology is often used in combination with Monte Carlo (MC) procedure to include uncertainties and stochastic input variables to study the stability and sensitivity of the space environment to different inputs. This allows for the computation of general statistics and probability density distributions for critical parameters. These models propagate single objects with high accuracy, thanks to high-fidelity dynamic models. However, they are computationally expensive and time-consuming to run, which does not allow us to analyze long prediction horizons. In addition, they are not generally publicly available. Examples of models employing this approach are LEO-to-GEO Environment Debris [11], Debris Analysis and Monitoring Architecture to the Geosynchronous Environment [12], and Debris Environment Long-Term Analysis [13]. The second methodology is based on source-sink models. These models rely on systems of coupled ordinary differential equations (ODEs) describing the evolution of the different species of ASOs involved, such as payloads, rocket bodies, and fragments [14]. Several discretizations can be introduced within those models, for example, in terms of species, orbital altitude, physical characteristics, and mass. Moreover, many phenomena can be modeled, like the orbital decay due to the atmospheric drag, new launches, collisions, explosions, and PMDs. The main drawback of these models is that information about single objects is missing because objects are propagated as species. However, these models are computationally fast and can provide essential information about the projected future distribution of ASOs in the space environment for a long prediction horizon. Although these debris models represent a typical approach employed to study the longterm evolution of the LEO population, some simplifying assumptions are often carried out, thus leaving room for further improvements to make these models more realistic and reliable and calibrate them against either truth data or data from MC simulations. Many works in literature have already employed source-sink models to study the LEO population. As an example, Kessler and Cour-Palais developed a model that considered the primary source and sink terms to study the evolution of the satellite population, predicting the significant growth of space debris due to collisions [15], with follow-on work by Kessler and Anz-Meador studying the stability of LEO using these modeling techniques based on empirical data and new breakup models [16]. Afterward, the results of that work were revised and investigated again with more recent data and new models [17], examining alternatives for controlling the future orbital debris environment. Furthermore, Talent [18] proposed a simple model based on one first-order ODE to describe the evolution trend of the objects in orbit. Finally, Somma et al. [19] introduced a feedback controller within a statistical source-sink model to investigate adaptable debris control strategies. The model developed by Somma [14] and called Model for Investigating control Strategies for Space Debris (MISSD) constitutes the baseline of the model exploited by Trozzi et al. [20] to study the evolution of the LEO region and analyze space environment capacity (including NT and the CSI). None of the works mentioned previously considered the presence of untracked debris among the objects species and a high-fidelity thermospheric density model as the JB2008.

This paper is organized as follows. First, the proposed sourcesink model is introduced together with the employed approach to consider the JB2008 thermospheric density model and the computation of some coefficients appearing in the model based on radar performances. Then, numerical analyses, including the spatial density and LEO orbital capacity, are presented and discussed. Finally, concluding remarks and future research directions are given.

II. Space Environment Model

The long-term evolution of ASOs is studied here through a multishell multispecies source—sink model. This model considers the subdivision of the LEO region into orbital altitude shells, assumed to be spherical, and takes into account three species of ASOs, namely, active satellites (S), capable of performing collision avoidance maneuvers; intact derelict satellites (D), which include disabled satellites and inactive satellites that fail to meet the PMD guidelines; and debris. The debris species is further divided into the following two groups: trackable (N) and untracked (U) debris. (Note that S, D, N, U are generally used throughout the paper to indicate the number of objects belonging to each specific population. However, when they appear as lowercase subscripts, they are just meant to be identifiers of each specific population.) The reason behind these subdivisions is related to the fact that our sensing capabilities are limited, both in terms of the number of sensors (optical telescopes and radars) and the technology. Therefore, tracking all the debris generated from collisions is impossible. For this reason, they represent a significant threat to the entire ASO population, especially to the active satellites, which are not always able to perform rapid collision avoidance maneuvers due to the nontrackability nature of untracked debris. Rocket bodies are not actively distinguished as its own species, and they are included as derelicts. Throughout the paper, the developed source–sink model will be referred to as MOCAT-4N, and it represents an improvement of the MOCAT-3 baseline model [21]. In particular, the number 4 indicates the number of species involved in the model, whereas N is related to the subdivision of debris into two subgroups. This is done to distinguish the different versions of the MOCAT models that the authors are currently developing. As already mentioned, source-sink models are based on a system of ODEs that describe the evolution and interactions of the species through time. Because the proposed model is multishell, the LEO is assumed to be divided into many altitude shells; therefore, the ASO population is computed for each altitude shell. Before introducing the equations, the assumptions considered to build the model are listed as follows:

- 1) Because spherical shells are considered, the model is valid for ASOs in near-circular orbit. Moreover, a nonrotating atmosphere is considered.
- 2) The model does not account for any perturbation but the atmospheric drag, which represents the only natural sinking mechanism of the model. This means that the semimajor axis is the only orbital element of ASOs that can change.
- 3) New active satellites are assumed to be directly injected into their final altitude orbit. They are not subject to drag decay effects because they are assumed to be able to perform station-keeping maneuvers.
- 4) Explosions are not modeled, as future technological improvements are expected to decrease their occurrences. Even when modeled, using a stochastic approach for the explosion rate as in [10,22], fragments are added such that the characteristics of past fragmentations are unchanged. Moreover, their occurrence is modeled as a monotonically decreasing probability after launch, which makes it hard to fit in source–sink models.

- 5) The current guideline of 25 years for PMD is not considered in this work, and active satellites are removed from the simulation after Δt years of operational life. This assumption corresponds to a favorable scenario; indeed, some companies are suggesting dismissing their constellation satellites within one year after their operational life [23].
- 6) The minimum size of both tracked and untracked debris that can disrupt an intact object is considered to be 10 cm. This value corresponds to the space surveillance network sensor historical detection limit [24]. Moreover, the physical characteristics of tracked and untracked debris are the same. One can note that, in this work, the adjective "untracked" or "nontrackable" is not linked to the size of the debris that is too small to be easily tracked (i.e., smaller than 10 cm), as commonly referred to in the literature. Indeed, untracked debris is used here to identify the debris that is not tracked because of the lack of sensor availability. As debris smaller than 10 cm can still represent a mission-ending hazard for small satellites, the threshold size assumption here assumed best fits the trackability analysis. Indeed, smaller untracked debris can be added to the model, at the cost of much higher computational cost, with the realization that they will probably never be detected by the sensors.
- 7) The number of fragments generated from the collisions is computed using the NASA standard breakup model [25]. For simplicity, we assume that the collision between intact objects, such as S S, S D, and D D, generates a catastrophic collision. In contrast, the collision with debris (both tracked and untracked) generates a noncatastrophic collision.
- 8) Any collisions involving untracked debris only produce untracked debris. Because of the lack of knowledge on how and when the collision involving the untracked debris occurred, it is assumed that the initially generated debris cloud due to these interactions is not tracked.
- 9) Average physical characteristics (mass, area, and diameter) are considered for each species, according to the median values proposed in Ref. [14].

A schematics representing the qualitative interactions among the species is illustrated in Fig. 1. As can be seen, the only source of the active satellite population is represented by the new launches. Therefore, the term that regulates the new launches is the annual launch rate, indicated with λ . At the same time, following the PMD guidelines, active satellites are removed from the simulation after Δt years of operational life. However, it is also likely that not all the active satellites succeed in performing PMD, thus becoming derelicts. This transition is considered by modeling the probability of success P_M of PMD. The other modeled phenomena are the collisions, the natural orbital decay caused by the atmospheric drag, and the interaction between tracked and untracked debris, which depend on the sensing capabilities. These three phenomena are explained in detail in the following subsections.

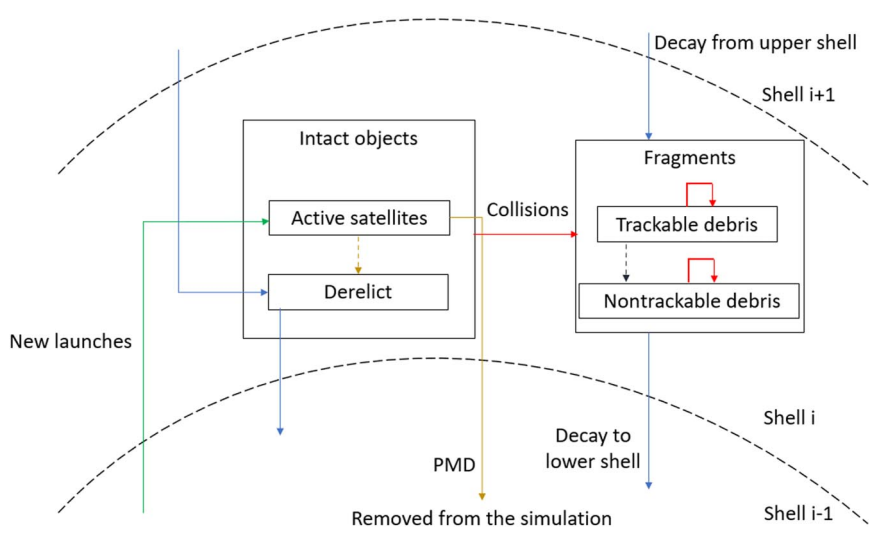


Fig. 1 Qualitative schematics of the MOCAT-4N model.

A. Collisions

To model the collision between the species involved in MOCAT-4N, some coefficients need to be introduced. The fractions of disruptive collisions with derelicts and tracked debris that an active satellite fails to avoid is referred to as α . On the other hand, the fractions of collisions with active satellites that an active satellite fails to avoid is represented by α_s . In particular, $\alpha_s < \alpha$ because collisions among active satellites are less frequent due to the collision avoidance capability of both the objects involved in the collision. Finally, δ is the ratio of the density of disabling to lethal debris; this term considers the possibility that disabling collisions can generate new derelicts. Instead, when the untracked debris are involved in the collision, the coefficients $\alpha_{\rm su}$ and $\delta_{\rm su}$ are employed. These last two coefficients are assumed to be higher than the respective counterparts, α and δ , because of the unpredictability of untracked debris. As already stated, collisions involving untracked debris produce only untracked debris (not tracked debris). For each pair of colliding ASOs, we can define the following variable related to the intrinsic collision probability [14]:

$$\phi_{ij} = \pi \frac{v_r(h)\sigma_{ij}}{V(h)} \tag{1}$$

where the subscripts i and j refer to the ith and jth species, respectively; $v_r(h)$ is the average relative velocity; V(h) is the volume of the orbital shell; h is the altitude; and σ_{ij} is the square of the impact parameter, and it is a function of the radius of the objects [14]:

$$\sigma_{ij} = (r_i + r_j)^2 \tag{2}$$

One can note that even though $v_r(h)$ is a function of the altitude, it is often considered equal to $v_r = \sqrt{2}v_c$, as it is done in this work, with v_c being the orbital speed at the average population altitude, with a value of 10 km/s for LEO [14]. Moreover, as it can be seen from Eq. (2), Eq. (1) is symmetric in the indexes i and j. Finally, the number of fragments generated from a collision between species i and j (K_{ij}) can be computed according to the NASA standard breakup model [25]. The following two different types of collisions are considered: catastrophic and noncatastrophic/damaging collisions:

$$K_{ii,c} = 0.1L_C^{-1.71}(M_i + M_i)^{0.75}$$
(3)

$$K_{ij,\text{nc}} = 0.1 L_C^{-1.71} (M_p \cdot v_{\text{imp}}^2)^{0.75}$$
 (4)

where L_C is the characteristic length of the minimum size of generated debris (assumed to be 0.1 m), $M_{i/j}$ is the mass associated to the colliding species i/j, M_p is the mass of the projectile (i.e., the mass of the less massive object, $M_p = \min(M_i, M_j)$), and v_{imp} is the impact velocity (assumed to be equal to 10 km/s). As mentioned before, collisions between intact objects are considered catastrophic, whereas collisions with debris are noncatastrophic.

To have a more compact form of the terms related to collisions, let \dot{C} be the vector expressing the terms related to collisions for each species:

$$\dot{\mathbf{C}} = [\dot{C}_s, \dot{C}_d, (1 - \xi)\dot{C}_n \cdot K, \xi \dot{C}_n \cdot K + \dot{C}_u \cdot K] \tag{5}$$

where K is the number of fragments generated by the collision, which is different for each pair of colliding species, and ξ is the fraction of untracked debris generated from a collision, and it will be explained more in detail in the next subsections of this paper. One can note that the terms \dot{C}_s , \dot{C}_d , \dot{C}_n , \dot{C}_u include both the additions and removals of objects related to each interaction event among the species for each ODE of MOCAT-4N. The components appearing in Eq. (5) can be expressed as

$$\dot{C}_i = \sum_{i=1}^{N_s} \Gamma_{ij} \phi_{ij} Q_i Q_j + \dot{C}_{\text{add},i}$$
 (6)

where $Q_{i/j}$ represents the number of objects of the generic species; $\dot{C}_{\mathrm{add},i}$ represents the gain in derelicts and debris and will be introduced later in this subsection; N_s is the number of species considered (in this work $N_s = 4$), $i, j = 1, \ldots, N_s$ are the subscripts indicating each species; and Γ_{ij} are the coefficients of the matrix Γ :

$$\Gamma = \begin{bmatrix} -\alpha_s & -(\delta + \alpha) & -(\delta + \alpha) & -(\delta_{su} + \alpha_{su}) \\ +\delta & -1 & -1 & -1 \\ +\alpha & +1 & +1 & 0 \\ +\alpha_{su} & +1 & +2 & 1 \end{bmatrix}$$
(7)

The matrix Γ identifies the coefficients involved in all the pair interactions among the species of objects, which indicates the fractions or the number of objects that are added/removed to/from each population. For example, the coefficient Γ_{11} regulates the interaction S-S, Γ_{12} the interaction S-D, and so on. Hence, each row of Γ refers to the coefficients included in the interaction terms of each ODE of the MOCAT-4N model. (The first row of Γ refers to \dot{S} , the second row to \dot{D} , the third row to \dot{N} , and the fourth row to \dot{U} .) The values of the coefficients are reported in Sec. III. Finally, the additional terms $\dot{C}_{\rm add,\it{i}}$ are the components of the following vector $\dot{C}_{\rm add}$:

$$\dot{C}_{\text{add}} = [0, +\phi_{sn}\delta SN + \phi_{su}\delta_{su}SU, +\phi_{sd}\alpha SD + \phi_{dd}D^{2} +\alpha_{s}\phi_{ss}S^{2}, 0]$$
(8)

where the terms ϕ are computed through Eq. (1). It is worth to mention again that the subscripts s, d, n, u are used in Eq. (8) as identifiers of the interactions considered.

B. Atmospheric Drag Effects

The atmospheric drag affects ASO semimajor axis, which continuously decreases, causing the natural orbital decay. This leads to a flux of objects decaying from the current shell to the shell immediately below. Indicating with Q the number of objects of a generic species, the flux due to the atmospheric drag $\dot{F}_{d,Q}$ can be written as

$$\dot{F}_{d,Q} = -\frac{Q_+ v_+}{d} + \frac{Qv}{d} \tag{9}$$

where d is the thickness of the shell, and $v = \dot{a}$ is the rate of change of the semimajor axis caused by the atmospheric drag. The subscript + indicates the quantities computed based on the values in the shell right above the one currently under analysis. The first term of Eq. (9) is related to the positive flux of objects entering the current shell, while the second term refers to the negative flux of objects leaving the current shell. Please, note that Eq. (10) has a minus sign. Moreover, the ratio d/v represents the residence time of the objects in the shell under analysis. Assuming near-circular orbits, for which $a \approx R_{\rm orb}$ (thus $\dot{a} \approx \dot{R}_{\rm orb}$), with $R_{\rm orb}$ being the distance computed from the center of Earth, and considering the orbital specific energy $\mathcal{E} = -(\mu/2a)$, where $\mu = 398,601~{\rm km}^3/{\rm s}^2$ is Earth's gravitational parameter, a the semimajor axis, m the mass of the spacecraft, v the spacecraft velocity, and F_D the atmospheric drag force, the time derivative of the specific energy yields:

$$\dot{\mathcal{E}} = \frac{\mu \dot{a}}{2a^2} = \frac{1}{M} \mathbf{F}_D \cdot \mathbf{v} = -\frac{1}{2m} \rho v^3 A c_D = -\frac{1}{2} \rho v^3 B$$

Hence

$$\dot{a} = -\frac{\rho v^3 a^2}{u} B$$

The rate of change of the semimajor axis, considering $v = \sqrt{\mu/a}$, is finally expressed as [14]

$$v = \dot{a} = -\rho B \sqrt{\mu a} \approx -\rho B \sqrt{\mu R_{\text{orb}}}$$
 (10)

where $B=c_D(A/m)$ is the ballistic coefficient, with c_D , A, and m being the drag coefficient, the area, and the mass of the object, respectively, whereas ρ is the atmospheric density. In this work, we are assuming $c_D=2.2$, which corresponds to the drag coefficient evaluated for a flat-plate model, an assumption usually carried out in literature [19]. Frequently, the atmospheric density is modeled with a static exponential model [20]. However, the atmospheric density is highly dynamic and can be strongly affected by time-varying factors, such as solar activity and geomagnetic storms. This is why the JB2008 thermospheric density model [4] is employed in this work.

The JB2008 thermospheric density model is a current state of practice for thermospheric mass density prediction. The JB2008 model has been validated via comparisons with accurate daily density drag data collected from satellites in orbit and has shown significant improvement compared to previous atmospheric density models. The JB2008 model uses a set of solar fluxes measured at different wavelengths and the temperature change due to the Disturbance Storm Time (DSTDTC) index as the main drivers for thermospheric density prediction. The set of solar fluxes captures the effects of the solar activities; meanwhile, the DSTDTC index captures the effect of the geomagnetic activities on the thermospheric density field.

One of the main challenges with the usage of the JB2008 atmospheric model for long-term prediction are the difficulties in accurately predicting the long-term solar and geomagnetic indices. In this work, the future solar and geomagnetic indices for the JB2008 density model are modeled based on the COSPAR International Reference Atmosphere 2008 [26]. The CIRA-08 provides the statistics of solar indices over a solar cycle with an average space weather activity. A solar cycle corresponds to the cycle that the sun's magnetic field goes through approximately every 11 years, which strongly influences the activity on the surface of the sun. The level of solar radiation, number of sunspots, solar flares, and coronal loops has shown periodic variation with the solar cycle. Using the mean, minimum, and maximum values within the CIRA-08 guideline, we fitted the following two Gaussian distributions

to the solar flux indices: a conservative low-variance model $[3\sigma_{\rm low} = {\rm min}(F_{\rm mean} - F_{\rm min}, F_{\rm mean} - F_{\rm max})]$ and a less conservative high-variance model $[3\sigma_{\rm high} = {\rm max}(F_{\rm mean} - F_{\rm min}, F_{\rm mean} - F_{\rm max})]$. The solar flux indices are assumed to evolve independently, sampled as independent Gaussian variables from one another at each time step. Meanwhile, the historical long-term mean value for the DSTDTC index of 58 K is used. For the analysis of this paper, the high-variance model has been employed. This assumption of a continuously moderate solar cycle over 200 years can result in inaccurate density predictions, as the solar cycle can alternate between periods of low activity and high activity. However, including the influence of the different solar activity levels still represents a better approximation of reality with respect to the static exponential model regarding atmospheric density.

The atmospheric density field can vary depending on the longitude and latitude; however, the MOCAT-4N model does not precisely propagate the space object in the three-dimensional (3-D) space and only models the population in distinct altitude shells. Thus, a mean density value is computed for each altitude shell using the JB2008 model and is then used to evaluate the mean drag force acting on all populations within the same altitude shell. The atmospheric density is computed by evaluating the JB2008 model over a 3-D grid with the spatial and temporal resolutions shown in Table 1. An average density for each altitude is then calculated by taking the mean over the two-dimensional latitude and longitude grid.

Figure 2 shows the variation in density at 600 km for different solar cycles (from 2020 to 2224) using the high-variance model. These estimated density variations better reflect the behaviors of the actual thermosphere under the different space weather conditions across the various solar cycles. Figure 3 shows the differences in predicted densities between the JB2008 density model and the static exponential atmospheric model. Under the different levels of space weather activity, the JB2008-predicted densities could vary by orders of magnitude. On the other hand, the static

Table 1 Spatial and temporal resolution of the JB2008 atmospheric density data

| | Domain | Resolution |
|----------------|-------------------------|------------|
| Longitude, rad | $[0; 2\pi]$ | 0.0698 |
| Latitude, rad | $[-0.49\pi; 0.49\pi]$ | 0.0684 |
| Altitude, km | [200; 2000] | 50 |
| Time | March 2020 to Feb. 2224 | Monthly |

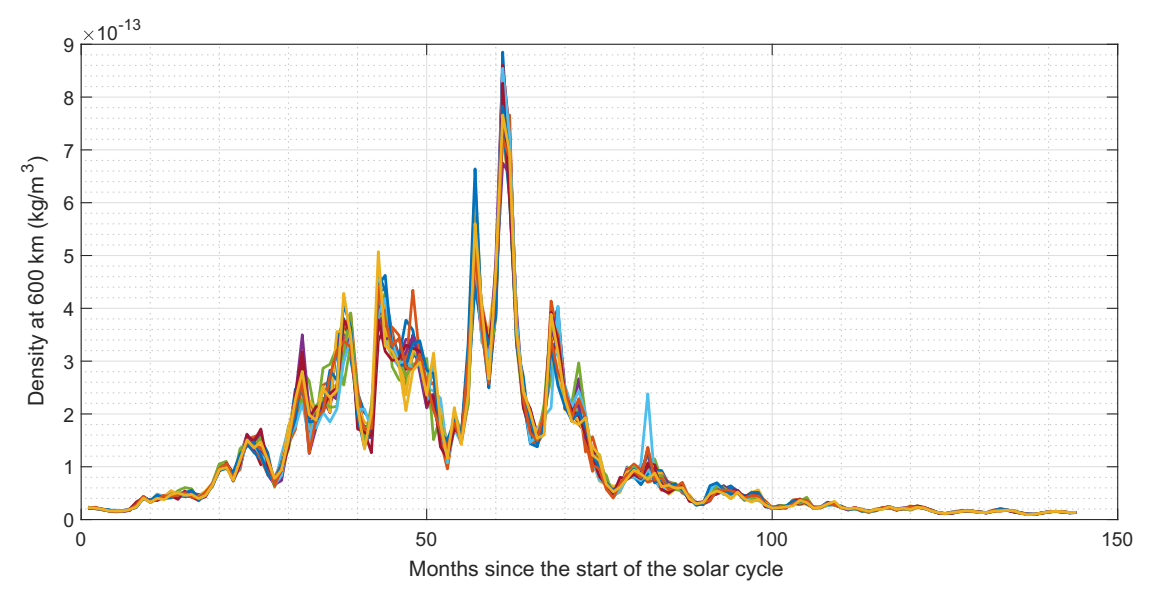


Fig. 2 Variation in predicted atmospheric density at 600 km over a solar cycle of approximately 11 years using the higher-variance model; the different colors of the plots represent different solar cycles.

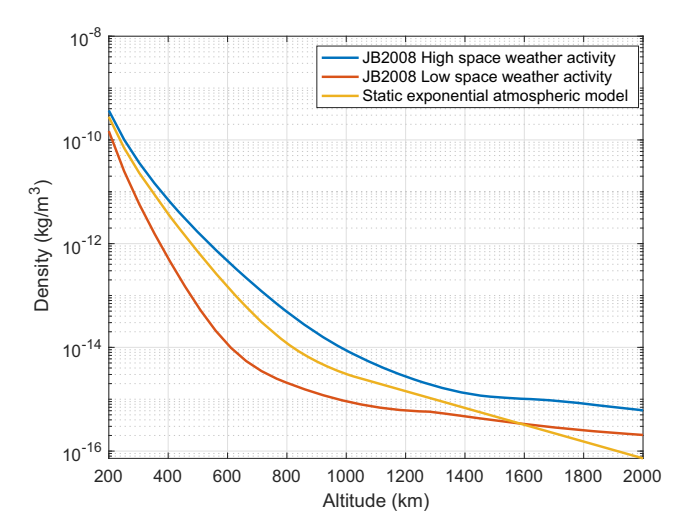


Fig. 3 Variation of density under different models and space weather activities.

exponential atmospheric model assumes a static atmospheric density regardless of the space weather activity [27]. The static atmospheric density overestimates the drag force under low space weather activity and underestimates the drag force under high space weather activity.

C. Interaction Between Tracked and Untracked Debris

To describe the interactions between tracked and untracked debris, three coefficients are introduced. The first one is $\xi(h)$ and represents the amount of untracked debris (with respect to the total number of fragments) generated from collision events. This is because we cannot track some debris because of poor coverage and sensor availability. In addition, it is altitude dependent, as the sensing capability of groundbased sensors generally decreases as the distance between the sensor and the objects increases. The other coefficients are $\gamma_n(h)$ and $\eta_n(h)$, representing the loss of custody of tracked debris and the successful tracking of untracked debris, respectively. These last two coefficients are also altitude dependent and related to the sensing capability; they describe how tracked debris can become untracked and vice versa. Because of the connection with the sensing capability, all three coefficients are estimated according to the probability of detection P_{det} , which is then further reduced by a percentage to consider that not all the objects detected are actually tracked. To retrieve the probability of detection, the signal-to-noise ratio (SNR) associated with radar has to be computed. The chosen reference radar model used has the characteristics reported in Table 2, whose parameters are taken from Ref. [28]. The SNR can be computed as [28]

$$SNR(R) = \frac{P_t G_t G_r G_p \lambda_w^2 \sigma_{RCS}}{(4\pi)^3 R^4 k T_s B_n L_s L_p}$$
(11)

where the system noise temperature is $T_s = T_0 \cdot \text{NF}$, $B_n = 1/\tau$, R represents the radar-object distance, and the other parameters are

Table 2 Radar parameters

| Parameter | Value | |
|--|---|--|
| Peak power P_t | 100 kW | |
| Transmitter antenna gain G_t | 40 dB | |
| Receiver antenna gain G_r | 40 dB | |
| Signal processing gain G_p | 13.3 dB | |
| Wavelength λ_w | 23.08 cm (L band) | |
| Transmitted pulse width with unmodulated waveform τ | 1 ms | |
| Noise temperature T_0 | 290 K | |
| Noise figure | 3 dB | |
| System loss L_s | 5 dB | |
| Propagation loss L_p | 1.2 dB | |
| Boltzmann constant k | $1.38 \cdot 10^{-23} \text{ m}^2 \cdot \text{kg} \cdot \text{s}^{-2} \cdot \text{K}^{-1}$ | |

introduced in Table 2. The only parameter that still needs to be obtained is the radar cross section σ_{RCS} . To estimate σ_{RCS} as a function of the object's size, the scattering regime must first be identified. The following three regimes exist: the optical regime, where the size of the object is much greater than the wavelength; the Rayleigh regime, where the size of the object is smaller than the wavelength; and the Mie or resonance regime, which is intermediate between the first two regions. In the Mie region, the radar cross section is oscillatory with frequency. By defining $x = b/\lambda_w$, where b is the diameter of the object, and $z = \sigma_{RCS}/\lambda_w^2$, the three regimes can be defined as

$$x = \begin{cases} \sqrt{\frac{4z}{\pi}} & \text{if } z \ge 5, \text{ optical regime} \\ \sqrt[6]{\frac{4z}{9\pi^5}} & \text{if } z \le 0.03, \text{Rayleigh regime} \\ g(z) & \text{if } 0.03 < z < 5, \text{ Mie regime} \end{cases}$$
 (12)

where for the Mie regime the smooth function g(z) can be obtained via numerical interpolation. In this last case, data from tables 3–6 of Ref. [29], reported in the Appendix and illustrated in Fig. 4, could be used for interpolation. Because we are interested in obtaining the radar cross section as a function of the object's size, Eq. (12) has to be inverted, and the regime is actually identified in terms of the circumference/wavelength ratio. If this value is smaller than 1, the object is within the Rayleigh regime; if it is higher than 10, the optical regime; and the Mie regime lies in between [30]. For example, if we consider debris with diameter b=0.3149 m and the wavelength in Table 2, the value of the circumference/wavelength ratio is about 1.57, which indicates a Mie regime. Therefore, by performing a linear interpolation of Fig. 4, we obtain $\sigma_{RCS}=0.0835\text{m}^2$.

Once the σ_{RCS} is evaluated, it can be substituted into Eq. (11). Hence, the probability of detection as a function of the range can be calculated as [28]

$$P_{\text{det}}(R) = 0.5 \cdot \text{erfc}(\sqrt{-\log(P_{\text{fa}})} - \sqrt{\text{SNR}(R) + 0.5})$$
 (13)

Table 3 Interactions among the species of the MOCAT-4N model

| | Species | S (active satellites) | D (derelicts) | N (tracked debris) | U (untracked debris) |
|--------------------------------------|---------|---|---|---|--|
| New launches Λ | | λ | 0 | 0 | 0 |
| Postmission disposal \dot{C}_{PMD} | | $-\frac{S}{\Delta t}$ | $\frac{(1-P_M)S}{\Delta t}$ | 0 | 0 |
| $\operatorname{Drag}\dot{F}$ | | 0 | ${\dot F}_{d,D}$ | ${\dot F}_{d,N}$ | $\dot{F}_{d,U}$ |
| Collision source \dot{C} | S | $-\alpha_s\phi_{ss}S^2$ | $\phi_{sd}\delta DS + \phi_{sn}\delta SN$ | $(1 - \xi)[K_{ns}\phi_{ns}\alpha SN + K_{ds}\phi_{ds}\alpha SD + K_{ss}\alpha_s\phi_{ss}S^2]$ | $\xi[K_{ns}\phi_{ns}\alpha SN + K_{ds}\phi_{ds}\alpha SD + K_{ss}\alpha_s\phi_{ss}S^2] + K_{nu}\phi_{su}\alpha_{su}SU$ |
| | D | $-\phi_{sd}(\delta+\alpha)SD$ | $-\phi_{dd}D^2$ | $(1 - \xi)[K_{dd}\phi_{dd}D^2 + K_{dn}\phi_{dn}DN]$ | $\xi[K_{dd}\phi_{dd}D^2 + K_{dn}\phi_{dn}DN] + K_{du}\phi_{du}DU$ |
| | N | $-\phi_{sn}(\delta+\alpha)SN$ | $-\phi_{dn}DN$ | $(1-\xi)[K_{nn}\phi_{nn}N^2]-\gamma_nN$ | $\xi[K_{nn}\phi_{nn}N^2]2K_{nu}\phi_{nu}NU+\gamma_nN$ |
| | U | $-\phi_{su}(\alpha_{su}+\delta_{su})SU$ | $\phi_{su}\delta_{su}SU-\phi_{du}DU$ | $+\eta_n U$ | $K_{uu}\phi_{uu}U^2-\eta_nU$ |

Table 4 Parameters employed for the simulations

| Parameter | Value |
|-----------------|----------|
| h_{\min} | 200 km |
| h_{\max} | 2000 km |
| $N_{ m shells}$ | 36 |
| d | 50 km |
| Δt | 11 years |
| v_r | 10 km/s |
| α | 0.2 |
| α_s | 0.01 |
| δ | 10 |
| P_M | 95% |
| c_D | 2.2 |
| L_C | 0.1 m |
| ξ% | 0.6 |
| γ% | 0.8 |
| η _% | 0.8 |

Table 5 Average physical characteristics of the ASOs (mass m, diameter b, and area A)

| ASO | m, kg | b, m | A, m^2 |
|-----------------------|-------|--------|----------|
| S (active satellites) | 1771 | 1.8512 | 4.5458 |
| D (derelicts) | 1771 | 1.8512 | 4.5458 |
| N (tracked debris) | 2.7 | 0.3149 | 0.6987 |
| U (untracked debris) | 2.7 | 0.3149 | 0.6987 |

where erfc is the complementary error function, and $P_{\rm fa}$ represents the probability of false alarm. Note that, in this work, the range R coincides with the altitude h. As an example, considering the values in Table 2, $\sigma_{\rm RCS} = 0.0835~{\rm m}^2$ and $P_{\rm fa} = 0.25 \cdot 10^{-3}$, the probability of detection as a function of the altitude $P_{\rm det}(h)$ is represented in Fig. 5. As expected, the probability of detection decreases as the altitude increases. However, for high altitudes, Eq. (13) could fail to provide a result because of the small SNR. For these altitudes, a small positive threshold for $P_{\rm det}(h)$ can be set to avoid numerical issues. As already mentioned, it is likely that not all the detected objects are successfully tracked. For this reason, the three coefficients required for the tracked and untracked debris interactions are formulated as

$$\xi(h) = 1 - P_{\text{det}}(h)\xi_{\%}$$
 (14)

$$\gamma_n(h) = 1 - P_{\text{det}}(h)\gamma_{n,\%} \tag{15}$$

$$\eta_n(h) = P_{\det}(h)\eta_{n,\%} \tag{16}$$

where $\xi_{\%}$, $\gamma_{n,\%}$, and $\eta_{n,\%}$ are values within the range (0,1) to decrease the value of $P_{\rm det}$ and relate detectability to trackability. Figure 6 provides better visualization of the interactions between tracked and untracked debris and the related coefficients. The coefficients $\xi_{\%}$, $\gamma_{n,\%}$, and $\eta_{n,\%}$ are related to the efficacy of the tracking technology, meaning that the higher the values of those coefficients, the more confidence and the better sensor capabilities we assume to have. The reader can choose the values of $\xi_{\%}$, $\gamma_{n,\%}$, and $\eta_{n,\%}$ according to the confidence in the technology (considering various aspects, such as sensor availability and sensor accuracy) and the instruments they

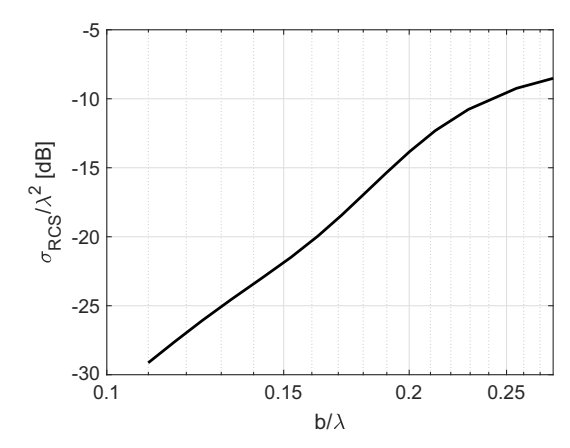


Fig. 4 Normalized radar cross section σ_{RCS} as a function of the normalized object size.

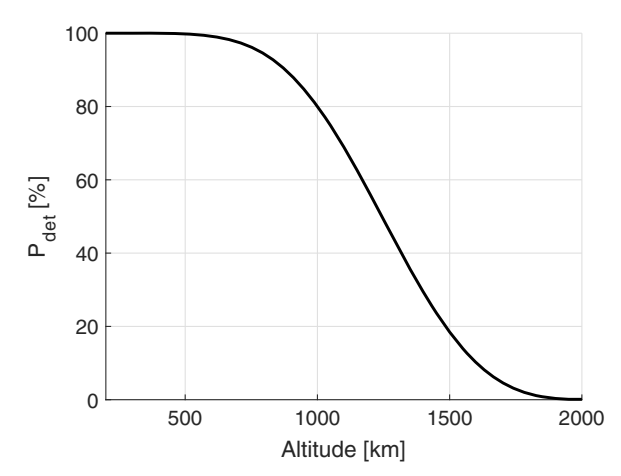


Fig. 5 Probability of detection as a function of the altitude for $\sigma_{RCS} = 0.0835 \text{ m}^2$ and $P_{fa} = 0.25 \cdot 10^{-3}$.

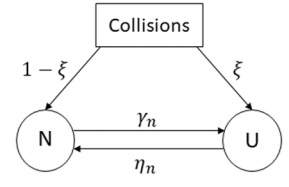


Fig. 6 Interactions between tracked and untracked debris.

consider. In addition, those coefficients could be related to the ratio of successfully tracked vs detected objects. However, the particular choice of the instrument is out of the scope of this work.

D. Final Model

To summarize, the final MOCAT-4N model, whose interactions are represented in Table 3, can be written in its explicit form as

$$\dot{S} = \lambda - S/\Delta t - \phi_{sd}(\delta + \alpha)SD - \phi_{sn}(\delta + \alpha)SN - \alpha_s\phi_{ss}S^2 - \phi_{su}(\alpha_{su} + \delta_{su})SU$$
(17)

Table 6 Comparison of the results with other source—sink models (the total numbers of fragments of Refs. [14,20] are the sum of collision and explosion fragments)

| | MISSD [14] (final population) | Trozzi et al. [20] (final population) | MOCAT-3 (final population) | MOCAT-4N (final population) |
|----------------|-------------------------------|---------------------------------------|----------------------------|-----------------------------|
| Intact objects | 5,103 | 3,478 | 6,328 | 6,345 |
| Fragments | 19,216 (14,973 + 4,243) | 19,730 (15,952 + 3,778) | 15,347 | 15,730 |
| Total | 24,139 | 23,208 | 21,675 | 22,075 |

$$\dot{D} = \frac{(1 - P_M)S}{\Delta t} + \phi_{sd}\delta DS + \phi_{sn}\delta NS - \phi_{dd}D^2 - \phi_{dn}DN$$
$$-\frac{D_+v_+}{d} + \frac{Dv}{d} + -\phi_{du}DU + \phi_{su}\delta_{su}SU$$
(18)

$$\dot{N} = (1 - \xi)(K_{ns}\phi_{ns}\alpha NS + K_{ds}\phi_{ds}\alpha DS + K_{nd}\phi_{dn}ND + K_{d}\phi_{dd}D^{2} + K_{s}\phi_{ss}\alpha_{s}S^{2} + K_{n}\phi_{nn}N^{2}) - \frac{N_{+}v_{+}}{d} + \frac{Nv}{d} + n_{n}U - \gamma_{n}N$$

$$(19)$$

$$\dot{U} = (\xi K_{ns})\phi_{ns}\alpha NS + (\xi K_{ds})\phi_{ds}\alpha DS + (\xi K_{nd})\phi_{nd}ND
+ (\xi K_{d})\phi_{dd}D^{2} + (\xi K_{s})\phi_{ss}\alpha_{s}S^{2} + (\xi K_{n})\phi_{nn}N^{2} - \frac{U_{+}v_{+}}{d}
+ \frac{Uv}{d} + K_{su}\phi_{su}\alpha_{su}SU + K_{du}\phi_{du}DU + 2K_{nu}\phi_{nu}NU
+ K_{u}\phi_{uu}U^{2} - \eta_{n}U + \gamma_{n}N$$
(20)

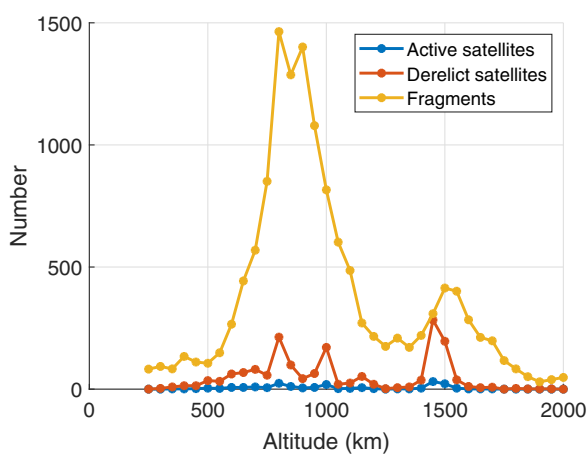
where the dependence on the altitude and time has been removed from the variables to simplify the notation. Note that the factor 2 in the N-U interaction term of the last equation appears because the two collision events N-U and U-N are considered probabilistically different.

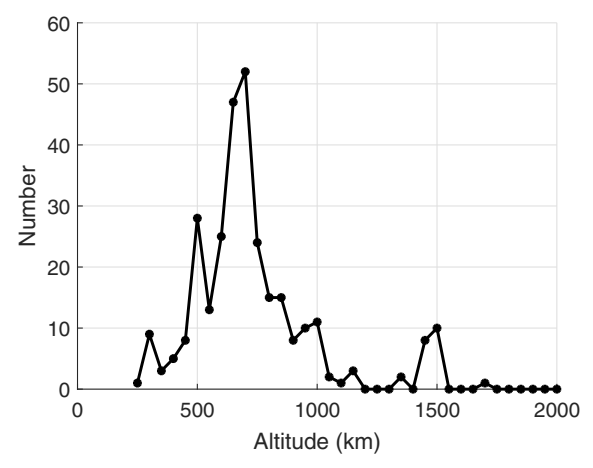
III. Numerical Results

In this section, numerical results are presented. For all the simulations, the probability of detection is computed considering the values of the radar illustrated in Table 2. The orbital altitudes analyzed in this work vary within the range 200-2000 km, divided into 36 orbital shells, each having a thickness of 50 km. The propagation time for the simulations is set to 200 years. The other coefficients employed to run the model are reported in Table 4, where a 95% success rate for PMD is assumed, and the operational lifetime Δt is 11 years. The reason behind the choice of this last value is mainly due to a compromise between the actual value of operational lifetime (usually 5-8 years) and the 25 year PMD guideline, because the reduction of ASO semimajor axis due to the PMD orbit reentry is not explicitly modeled in this work. The values of the other coefficients in Table 4 are taken from Ref. [31]. Moreover, $\alpha_{su}=2\alpha$ and $\delta_{su}=2\delta$. The average physical characteristics of the ASO species are shown in Table 5, where the values are taken from Ref. [20]. To compare the results of the MOCAT-4N model with respect to other source-sink models available in the literature, several simulations are carried out. The yearly launch rate, taking into account a business-as-usual scenario (i.e., no significant changes in the launch activities), and the initial distribution of the population are considered the same as in Refs. [14,20], where data have been extracted from the Meteoroid and Space Debris Terrestrial Environment Reference (MASTER) 2009 data set [32] with a reference epoch of 9 May 2009 and illustrated in Fig. 7. In particular, 90% of the initial number of satellites have been considered inactive satellites, thus derelicts, and 10% active satellites. This assumption is mainly carried out for compliance and comparison purposes with Ref. [14], where pre-constellation launch traffic was considered. However, the ratio of active vs inactive satellites has significantly changed in recent years due to the high presence of mega-constellation; thus, this assumption does not reflect the current population scenario. The initial distribution of debris for the MOCAT models is assumed to be the sum of collision and explosion fragments from Ref. [14]. Three different analyses are performed and presented as follows. The first analysis is useful to compare the MOCAT-4N model with the baseline MOCAT-3 model introduced in Ref. [21]. This allows us to understand the differences in the evolution of ASOs if untracked debris are considered. The second analysis compares the results of MOCAT-4N with the ones obtained from the MISSD model employed in Refs. [14,20] to test the fidelity of the proposed model. Hence, the last analysis is related to the prediction of the space environment evolution employing an updated initial population, which is the reference population of 2016 taken from MASTER-8.0.3 [33]. Moreover, estimation of orbital capacity is provided according to the metrics mentioned previously (NT product and CSI).

A. Comparisons with Other Source-Sink Models

To compare the MOCAT-3 and MOCAT-4N models, with the latter differing from the former just for the division of the debris species into tracked and untracked debris, the JB2008 thermospheric density model has also been implemented in the MOCAT-3 model, instead of the static exponential density model [27], to perform a fair comparison. In particular, the initial debris population adopted for MOCAT-3 is split into 80% of tracked debris and 20% of untracked debris for the MOCAT-4N model. By doing so, we can understand what happens to the final ASO population if we consider part of the initial population of debris as untracked. The coefficient $\xi_{\%}$ is considered a fixed value equal to 0.6, meaning that each collision generates 60% of tracked debris. (This value can be further studied in future works according to the confidence of our sensing capabilities.) However, this value is compliant with the approach employing the Henize factor considered in the ESA-MASTER v8.0.0. final report [34]. While $\xi_{\%}$ is considered a fixed value, a sensitivity analysis is performed to understand how the coefficients $\gamma_{\%}$ and $\eta_{\%}$ affect the results. A grid $\gamma_{\%}$ - $\eta_{\%}$ has been created with the following parameters: [0.5; 0.9] \times [0.5; 0.9] with step 0.05. The results of this test are shown in Fig. 8, where the difference between the total number of debris of MOCAT- $4N [(N + U)_4]$ and MOCAT-3 (N_3) is plotted as a function of $\gamma_{\%}$ and $\eta_{\mathcal{O}_{h}}$. As can be observed, if untracked debris are considered, the final population of debris is higher than if only tracked debris are considered. This proves the necessity of considering this species within





a) Distribution of the initial population

b) Yearly launch rate

Fig. 7 Initial conditions taken from Ref. [14].

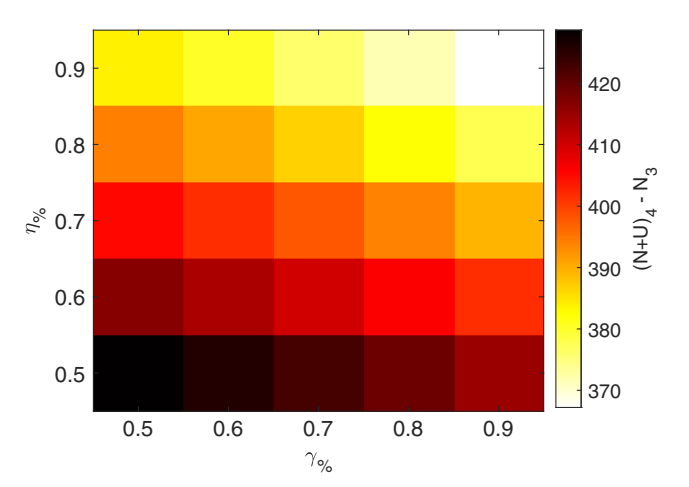
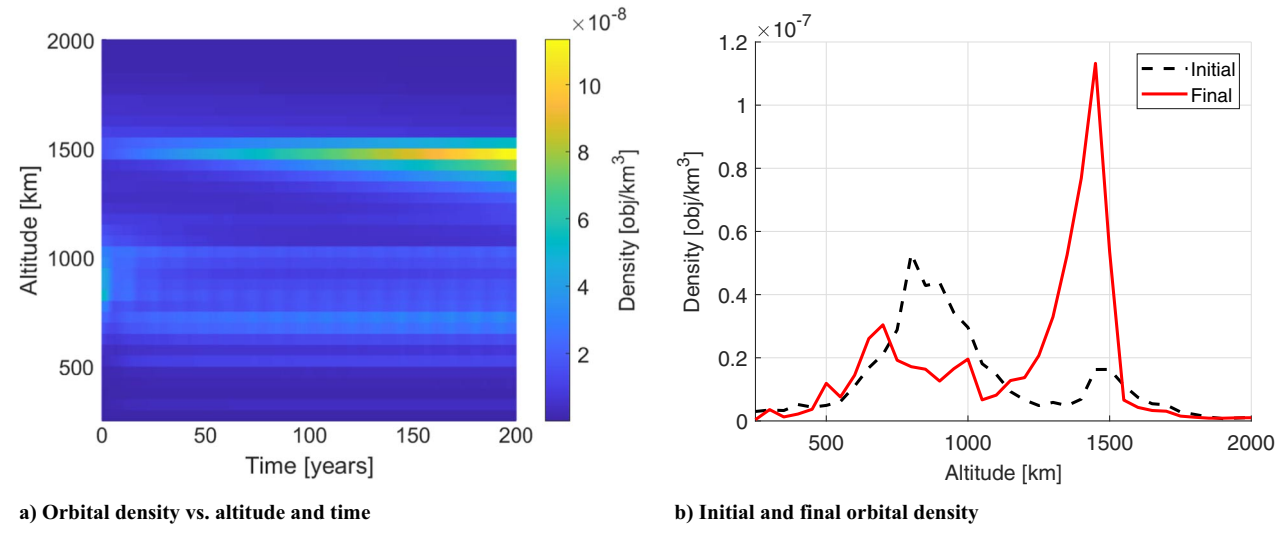


Fig. 8 Sensitivity analysis of the MOCAT-4N coefficients for the tracked-untracked debris interaction.

source–sink models not to underestimate the debris population. Moreover, a greater difference between the predictions of the two MOCAT models occurs for lower values of those coefficients. Indeed, the low value of $\gamma_{\%}$ indicates that there is a higher loss of custody (higher γ_n), whereas a low value of $\eta_{\%}$ means that the sensing capability of our technology is not good enough to detect and track the untracked debris. For the rest of the analysis of this paper, it has been chosen

 $\gamma_{\%} = \eta_{\%} = 0.8$. More studies regarding the influence of these coefficients with respect to the capability of the current or future technology will be performed in future works.

With the chosen values of the coefficients describing the interactions between tracked and untracked debris, the results of the propagation of the MOCAT models are illustrated in Figs. 9 and 10 and Table 6. Figure 9a shows the trend of the orbital density, considering all the ASOs, as a function of time and for each altitude shell. As shown in Fig. 7a at the beginning of the propagation, two peaks of the orbital density can be identified in the altitude shells around 800 and 1500 km. Indeed, the first peak is due to the fragments produced by the collision between Iridium 33 and Cosmos 2251 satellites, which occurred on 10 February 2009. Meanwhile, the second peak is mainly due to an explosion that occurred about four decades ago [20]. After 200 years of propagation, the first peak decreases, thanks to the atmospheric drag, whereas the highest peak shifts to higher shells where the decay effects are not strong and objects tend to accumulate, causing collisions and debris generation. This explanation is also supported by Fig. 10b, where the peak in the debris around 1500 km is clearly visible. Moreover, it is possible to observe from Fig. 10b that, even though the total numbers of both tracked and untracked debris globally increase (see the results of the propagation in Fig. 10a), at the end of the simulation time the number of untracked debris is greater than the number of tracked debris in high altitude shells. This behavior is expected due to the limitation in the sensing capabilities, which worsen with respect to the increasing altitude. The results illustrated in Fig. 10a also show that the evolution of untracked debris



g. 9 Orbital density obtained via the MOCAT-4N propagation.

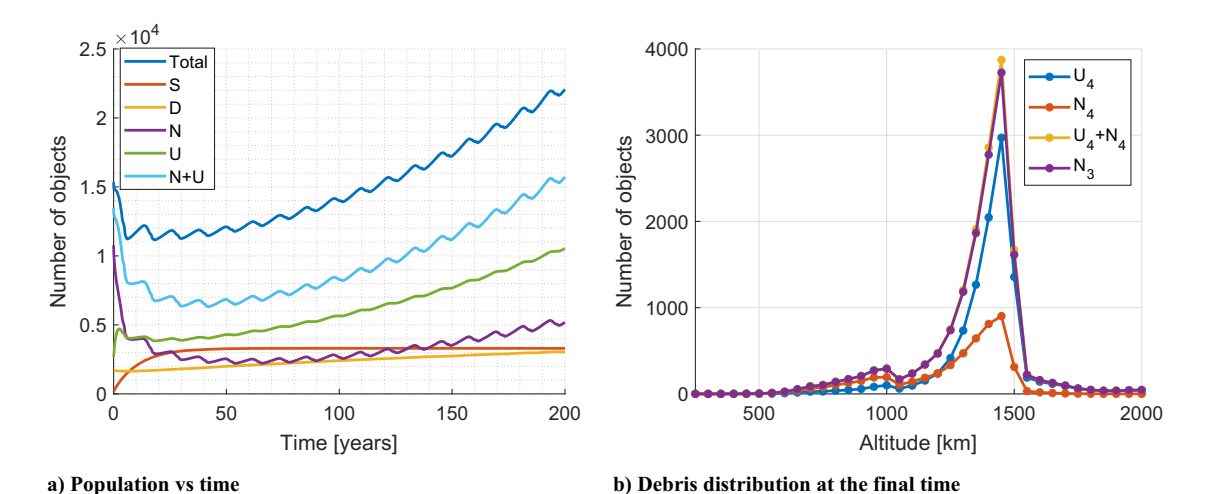


Fig. 10 Results obtained via the MOCAT-4N propagation.

does not present an evident oscillatory trend, as instead perceived by the tracked debris evolution, because untracked debris mainly reside in high altitude shells where the atmospheric drag does not play a key role for the orbital decay. (Thus, it is not significantly affected by the space weather.) From the comparison with MOCAT-3, it can be seen that it is important to consider untracked debris because the total number of debris is greater for MOCAT-4N, thus causing a greater probability of collisions with more debris and derelict generation and a lower number of active satellites (decreasing the overall available capacity).

To test the predictions of MOCAT-4N with respect to previous results obtained with other source-sink models introduced in the literature, a comparison with the MISSD model is performed. This model, first introduced by Somma [14], has also been exploited with some modifications by Trozzi et al. [20], employing, however, a static density model to study different LEO environmental capacity metrics. To perform the comparison, the initial population of both collision and explosion fragments considered in the other works is here summed up to build the generic family of debris (divided into 80% of tracked debris and 20% of untracked debris). Moreover, the initial populations of rocket bodies and mission-related objects are neglected for the analysis. The results are illustrated in Table 6. The reader has to note that in Table 6, intact objects are meant to be the sum of active satellites and derelicts for the MOCAT-4N model, whereas in the other models they are the sum of active payloads, inactive payloads, rocket bodies, and mission-related objects. For this reason, a precise comparison cannot be performed; however, the proposed comparisons are still useful to validate the order of magnitude of the total number of objects obtained with the MOCAT-4N model. It is possible to see that the proposed model predicts a lower population of ASOs than the other approaches. Between MOCAT-3 and MOCAT-4N, there is a good agreement on the prediction of the final population, with a difference of 400 objects, but the result can vary depending on the choice of the coefficients $\xi_{\%}$, $\eta_{\%}$, and $\gamma_{\%}$. Moreover, it is worth highlighting that in MOCAT-4N, the number of active satellites at the final time is slightly lower than in MOCAT-3, whereas the number of derelicts is higher. This is expected because more debris, and thus collisions, are generated. As a last remark, the difference in the results with respect to MISSD and the model employed in Ref. [20] is due to many reasons, such as different species of ASOs, different solar flux data and models, different PMD policy implementation, different physical characteristics varying according to both species and altitude that affect collisions and the orbital decay, and the presence of a corrective factor for the collisions for the case of the MISSD model.

For the analyzed scenario with MOCAT-4N, the following two metrics to compute the orbital capacity are considered:

1) The NT product, introduced by Krag et al. [6], relates the total available capacity to the integral of the curve resulting from the difference in the trend of fragments produced in two different scenarios over 200years. The first scenario is based on the assumption of a business-as-usual scenario, and the second one considers no additional launches.

2) The second metric is an analytical index, called CSI, proposed by Rossi et al. [7]. This index is associated with inactive large and abandoned objects, which represent a threat to the space environment and produce large debris clouds. It is based on many factors, including background debris density, orbital lifetime, mass, and orbital inclination, and it is defined as

$$CSI = \frac{M(h)}{M_0} \frac{D(h)}{D_0} \frac{\text{life}(h)}{\text{life}(h_0)} \frac{1 + k\Gamma}{1 + k}$$
 (21)

with M being the mass of the object, D the spatial density, life(h)the altitude-dependent residual lifetime of the object, $\Gamma =$ $(1 - \cos(i))/2$ takes into account the inclination of the object, and k = 0.6, considering the fact that usually the flux of debris on a nearequatorial orbit is about 60% of the flux of a polar orbit. All the other parameters with the subscript 0 refer to normalizing values. The lifetime of an object can be approximated with the following law [20]: $\log(\text{life}) = 14.18 \ h^{0.1831} - 42.49$. The reference values are $M_0 = 10,000 \text{ kg}, h_0 = 1000 \text{ km}, \text{ life}(h_0) = 1468 \text{ years}, \text{ and } D_0$ is the maximum spatial density evaluated using the initial distribution of the population and the volume of each shell ($D_0 = 5.2910 \times 10^{-8}$ for the current test case and $D_0 = 5.1000 \times 10^{-8}$ for the next scenario with the updated initial population [33]. It is also essential to notice that the greater the value of CSI is for an object, the more dangerous that object is to the environment. Furthermore, the variation of the cumulative CSI index over a long-time span can be used as an indicator of the trend in the use of capacity [20].

The result of the NT metric is shown in Fig. 11a, with a value of NT = 359,264 (green area), which corresponds to an average annual capacity of NT $_y$ = 1796, displayed with a red line in the figure. This value is coherent with what was reported by Krag et al. [6]. As mentioned previously, the NT value comes from integrating the difference in the number of fragments evaluated considering launches over the number of fragments calculated considering no additional satellites are launched into orbit. Looking at the figure, it can be seen that both curves, blue for the launch-less propagation and magenta for the prediction with launches, increase over time. While the second scenario is expected due to the greater population in orbit, the increasing trend even without any additional launches is mainly due to the collisions among derelicts and debris that occur at high altitudes with a conse-

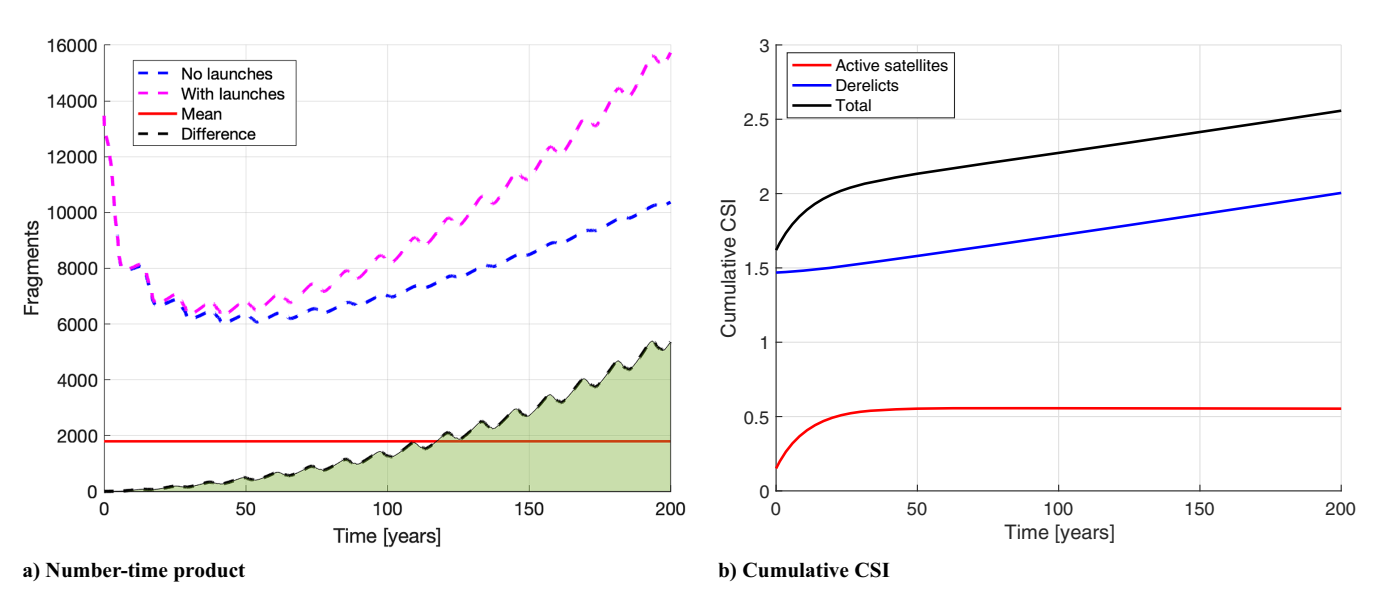


Fig. 11 Orbital capacity metrics for the MASTER initial population.

quent increase in the debris population. This can be deducted from the nonoscillatory behavior of the blue curve because, at high altitudes, the drag forces acting on the ASOs are minimal because of the low atmospheric density. The lack of strong oscillations is indeed related to a null launch rate; without new objects launched at low altitudes, there are no collisions that produce further derelicts and debris, which are subject to the strong orbital decay due to the atmospheric drag influenced by the space weather. Figure 11b shows the cumulative CSI and the two components related to active satellites, in red, and derelicts, in blue. After a short transient, where the satellite CSI stabilizes, the total CSI linearly increases due to the increase of derelicts. The CSI directly correlates to the safety of the LEO space environment, as a higher CSI value corresponds to a higher risk. Therefore, Fig. 11b underlines the necessity of active debris removal of derelicts and rigorous policies for PMD, with the lowest achievable percentage of failure. Indeed, even with the constant increase of space debris, derelicts will continue to be the main source of risk for orbit capacity.

1. Evolution of ASOs Under Different Atmospheric Models

A longer time horizon propagation of 300 years has been carried out to better study the effect of the different atmospheric models on the ASO evolution. The same initial conditions as those represented in Fig. 7 were used for both scenarios. Figure 12 shows the evolution of the different ASO populations under the static exponential density model and the JB2008 density model. The evolution

of the ASO populations follows a similar trend for both scenarios. However, the ASO populations under the JB2008 density model show an oscillatory behavior. In addition, it can be observed that the difference between the two models increases with propagation time.

Figure 13 shows the percentage difference between the ASO populations under the two different atmospheric models. The percentage difference is calculated using the following equation:

$$\Delta_{Q,t} = 100 \frac{Q_{\text{exp}} - Q_{\text{JB2008}}}{Q_{\text{exp}}} \tag{22}$$

where $Q_{\rm exp}$ and $Q_{\rm JB2008}$ are the total number of objects of a generic species at the current time using the exponential density model and the JB2008 atmospheric model, respectively. The percentage difference between the two models can be as high as 20%, which motivates the need for a time-varying atmospheric density model to better capture the effect of the solar cycle for orbital capacity analysis.

B. Evolution of ASOs Under an Updated Initial Population

After MOCAT-4N has been tested against previous models, it is now employed to study the evolution of the space environment, considering a new updated initial population corresponding to the year 2016, taken

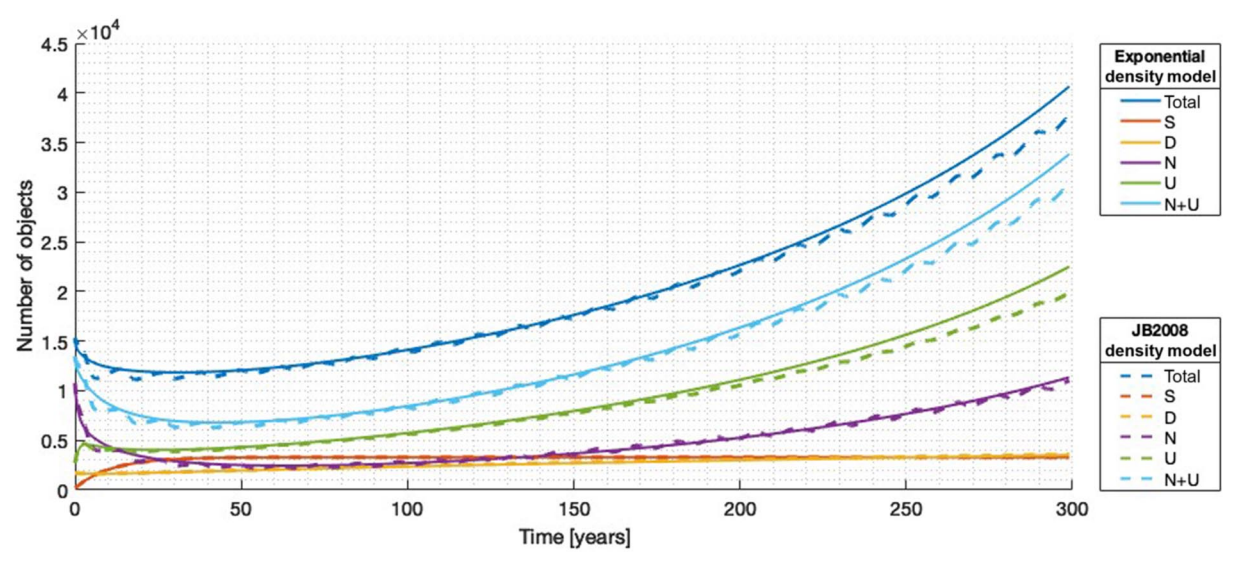


Fig. 12 Evolution of ASO under different atmospheric models.

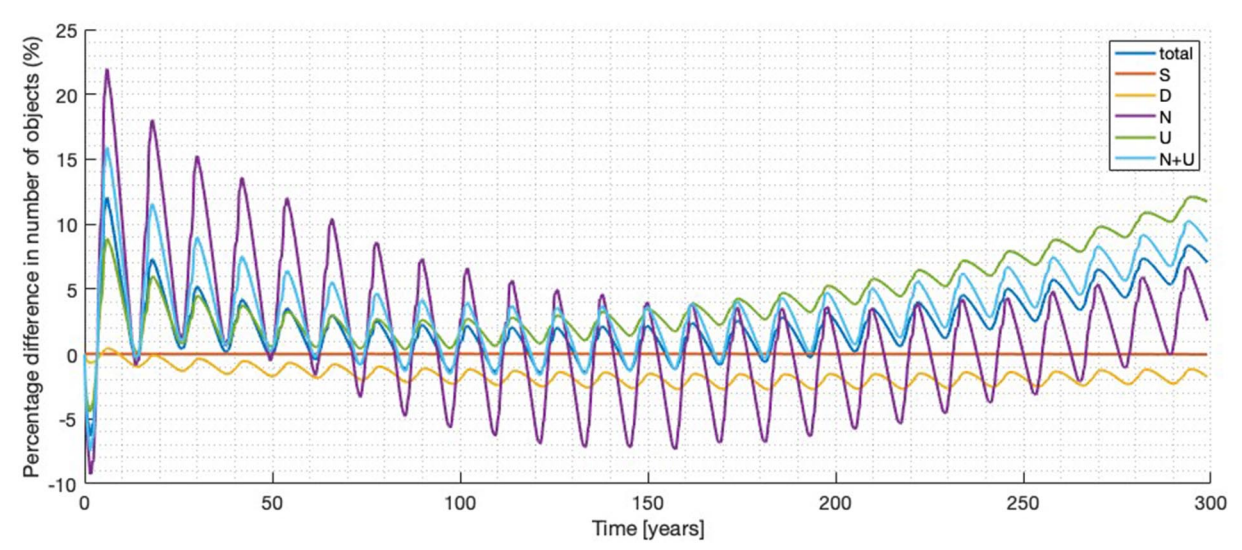


Fig. 13 Percentage difference in ASO populations under different atmospheric models.

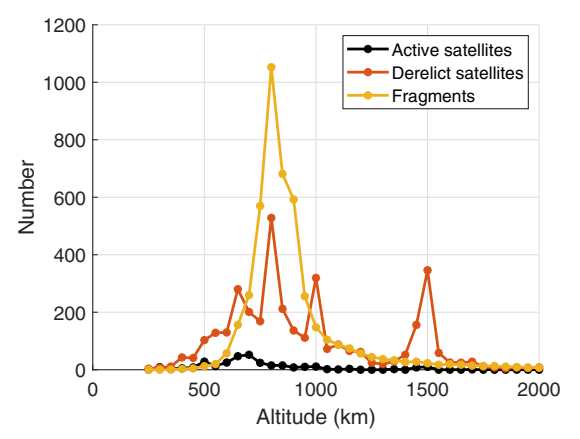


Fig. 14 Distribution of the initial population of 2016 taken from MASTER-8.0.3.

from MASTER-8.0.3. In particular, collision fragments and launched objects are directly obtained through MASTER. The initial population distribution over the altitude shells is illustrated in Fig. 14. However, 90% of the initial population of satellites is assumed to be derelict. (A similar assumption was used for the inactive payload population by Somma [14].) The rest is considered active satellites. For what concerns the subdivision of tracked and untracked debris, 20% of the initial population of collision fragments is assumed to be untracked

debris, and the rest (80%) is tracked debris. The yearly launch rate is the same as the one employed in the previous simulations and shown in Fig. 7b, assuming a business-as-usual scenario. The results are presented in Figs. 15 and 16. For the orbital density, the same considerations made in the previous scenario are still valid. However, an increase in the total number of ASOs residing in LEO can be highlighted, as seen in Figs. 15 and 16a. The increase is mainly due to the derelicts and debris population. Higher peaks in the debris species at the final time can be observed in Fig. 16b. This simulation with the initial population related to 2016, and thus with pre-constellation launch traffic, proves the already increasing trend of ASOs we would be facing over the years. Furthermore, considering the more recent constellations of satellites would lead to an even greater number of ASOs in orbit, with a higher probability of collision. Indeed, in the 2016 scenario simulation, we reach 24,809 objects after 200 years, which is higher than the number found in the previous analysis. The peak of the orbital density around 1500 km of altitude is also consistent with the results obtained by Trozzi et al. [20]. Even for this test case, the number of debris from MOCAT-4N (about 17,250) is higher than the number of debris obtained via MOCAT-3 (about 16,700), as illustrated from the comparison in Fig. 16b.

The NT and the CSI metrics are computed and shown in Fig. 17. The new NT value for the selected time period is NT = 476,725, which corresponds to an average annual capacity of NT $_y$ = 2384. As can be seen, these results are higher than in the previous case, and this is due to the higher initial number of derelicts for this current scenario. However, the NT shows a similar behavior with

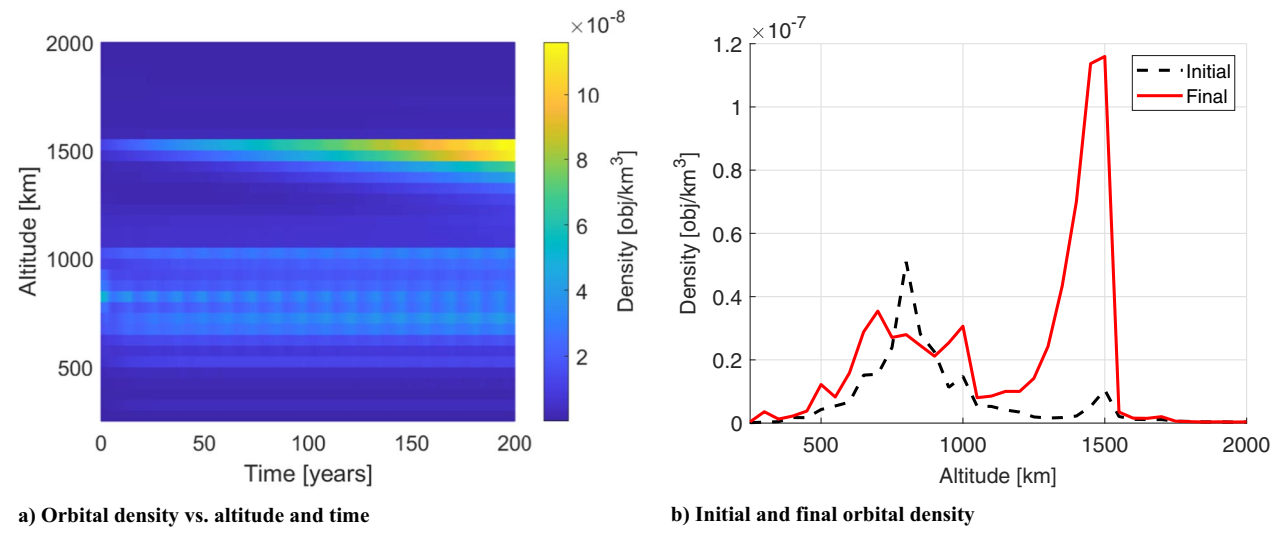


Fig. 15 Orbital density obtained via the MOCAT-4N propagation (MASTER-8.0.3).

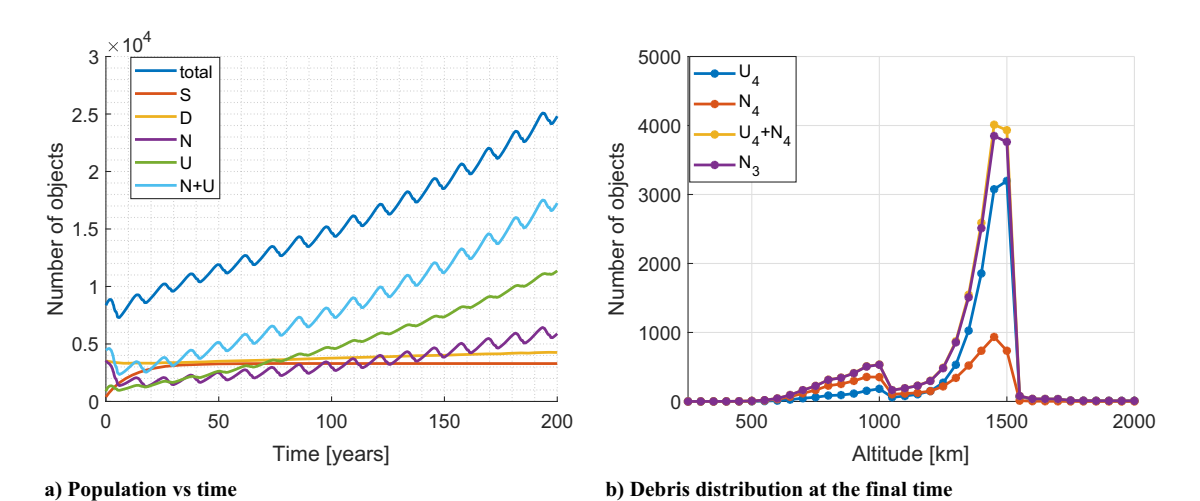


Fig. 16 Results obtained via the MOCAT-4N propagation (MASTER-8.0.3).

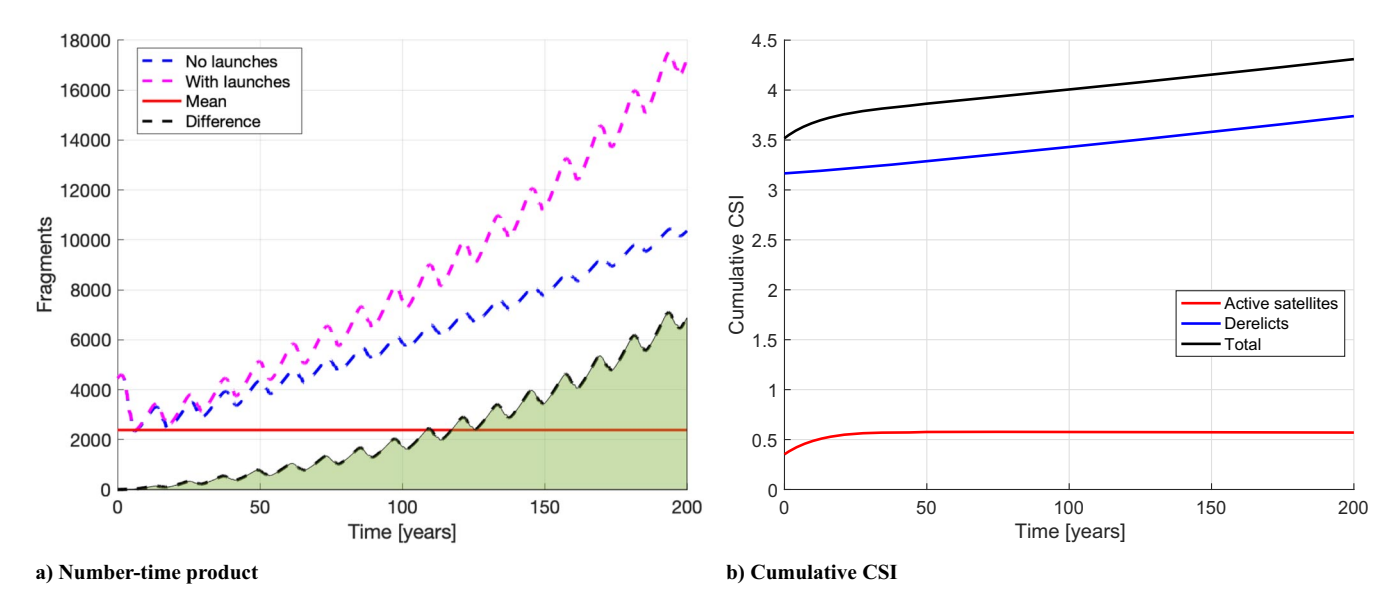
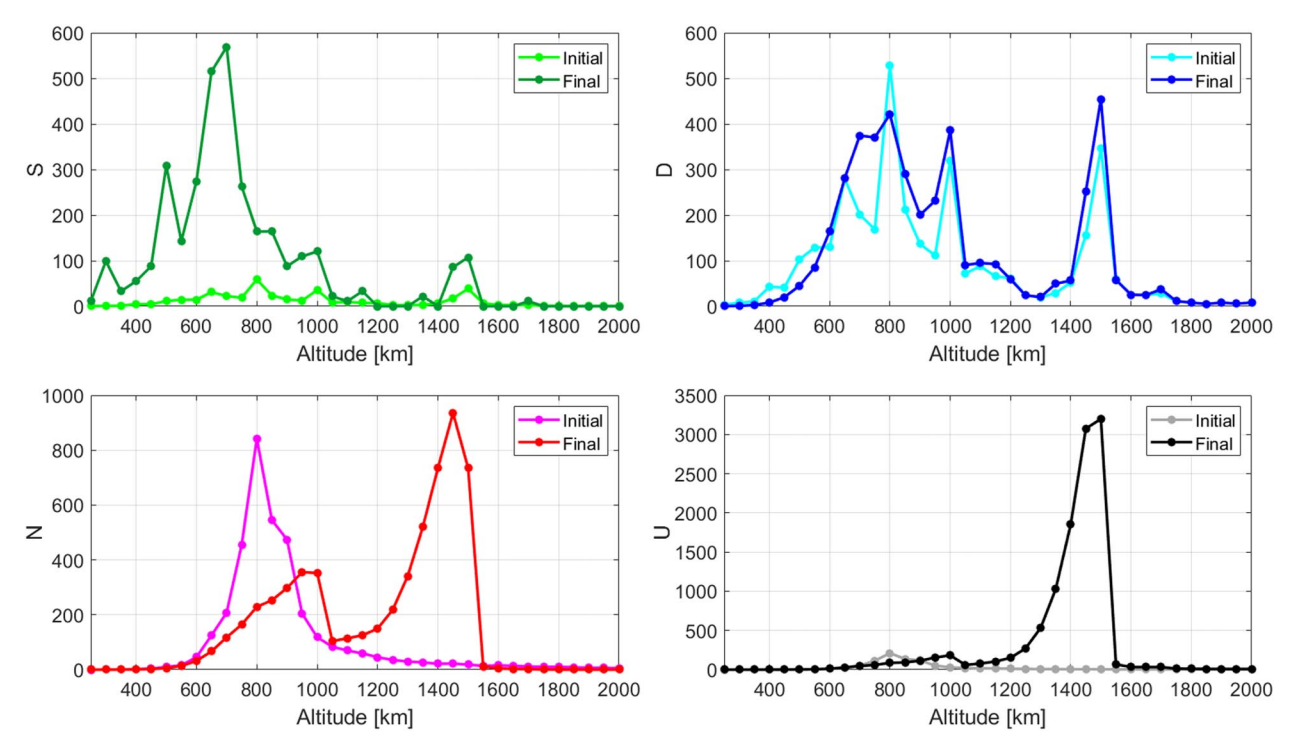


Fig. 17 Orbital capacity metrics for the MASTER initial population.

respect to the previous case, with a similar pattern among the curves. The average NT per year is higher than in the previous case, which is also consistent with the new values of CSI. Indeed, the cumulative CSI, illustrated in Fig. 17b, is much higher than the one computed with the previous population. When comparing the two figures, Figs. 11b and 17b, it can be noted that the CSI contribution from the derelicts is the main difference between the two sets of data.

A direct comparison between the initial and the final population is provided in Fig. 18. The four different families of space objects are portrayed separately. As predicted and expected, the number of active satellites drastically increases, especially around the 600–800 km range, leading to a peak in the derelict population around the same altitudes. However, the derelict population shows its maximum around 1500 km. When analyzing the time behavior of each population along the 200 years duration of the simulation, the cause of such peak is connected to collisions and debris creation. When a satellite collides at relatively high altitudes, the generated debris do

not decay fast enough to avoid new collisions. As such, a cascade effect occurs, and that altitude fills up with either tracked or untracked debris. Consequently, the number of untracked debris is also particularly elevated around 1500 km because the probability of detection is lower for such high altitudes. The most informative behavior comes by looking at the tracked debris family. In the first years of the simulation, the peak of the initial population, the magenta line, rapidly decreases due to orbit decay. At the same time, as collisions start to occur between derelicts, a new mode starts to arise at 1500 km, and its magnitude constantly increases for the whole simulation. The number of tracked debris below 1000 km shows a periodic behavior due to the space weather activity. The red hump in Fig. 18 lowers and increases its amplitude following the 11 years solar cycle. If we were to display the number of debris during a period of high space weather activity, we would notice the flattening of the hump. On the contrary, it enlarges in years of low solar activity. This "breathing" phenomenon of the N population explains the periodic components of the curves shown in Figs. 16a and 17a.



 $Fig.\ 18\quad Initial\ vs\ final\ population\ for\ the\ MASTER\ initial\ population.$

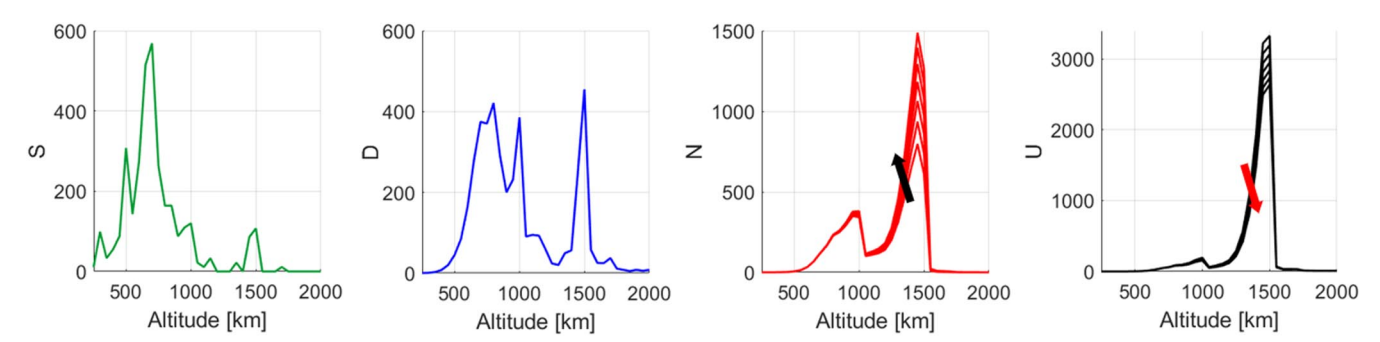


Fig. 19 Final populations at different radar capabilities; the arrows represent the direction of increasing peak power.

C. Evolution of ASOs Under Different Radar Capabilities

A sensitivity analysis of the predictions of the MOCAT-4N source-sink model was conducted by varying the radar's peak power between 90 and 150 kW. It is important to remember that the previously presented analyses employed a radar's peak power value of 100 kW. The increase in the radar's peak power is a synonym for improving detection capability, as the detection probability of the debris is directly proportional to the radar's peak power. Thus, this analysis assumes a technological improvement in the near future, where more powerful radars will be developed for debris detection. Figure 19 shows the variation of the final population under different radar capabilities. The increase in the radar's peak power does not significantly impact the active satellite population, as most of the active satellites lie below 750 km, where there is a very high detection probability in all cases considered. The final population of the derelicts remains constant across all test cases, as derelicts cannot conduct maneuvers to avoid untracked debris. However, we can detect (and track) more untracked debris at altitudes greater than 750 km with increasing radar's peak power, which causes a decrease in the number of untracked debris and a corresponding increase in the tracked debris population, increasing the safety of the overall LEO

IV. Conclusions

This paper focused on the development of MOCAT-4N, which is a multishell multispecies source-sink model, including a dynamic atmospheric density based on the JB2008 model, to study the evolution of ASOs in LEO. Apart from active satellites and derelicts, a new species, the untracked debris, has been introduced with respect to the MOCAT-3 model. Untracked debris represent a significant threat in the space environment because they are not tracked. For that reason, it is more difficult for active satellites to perform collision avoidance maneuvers. The new terms modeling the interactions between tracked and untracked debris rely on the computation of the probability of detection based on typical radar parameters. The results have shown that the population of debris obtained via MOCAT-4N is generally higher than the one retrieved by the original three-species MOCAT-3 model, which is reasonable because of the presence of untracked debris. Moreover, the comparison with another source-sink model in the literature, the MISSD model, shows good agreement in estimating the population. Thus, the effectiveness of the proposed model in evaluating the evolution of ASOs has been proved through simulations and comparisons with other approaches in the literature. MOCAT-4N has also been used to predict the evolution of the ASOs according to a new updated initial population obtained through the MASTER database, showing an increasing trend of the debris population during the years. Furthermore, the orbital capacity, in terms of the NT product metric and the CSI, has been computed for each simulation. A sensitivity analysis performed on the final predicted population as a function of the radar's peak power has shown that a better safety of the overall LEO environment can be achieved with more powerful radar technology, decreasing the untracked debris population in favor of the tracked one. Future works will consider the validation and calibration of the model with MC analysis; the introduction of additional species of objects, especially rocket bodies; and different discretizations of physical characteristics of ASOs.

Appendix: Mie Scattering Regime Data

The data expressing the relation between z and x = g(z) for the Mie scattering regime, as obtained from tables 3–6 of Ref. [29] and illustrated in Fig. 4, are here reported in Table A1 for completeness.

Table A1 Values of x and z representing the Mie scattering regime (reproduced from tables 3–6 of Ref. [29])

| $x = b/\lambda$ | $z = \sigma_{\rm RCS}/\lambda^2$ |
|-----------------|----------------------------------|
| 0.10997 | 0.001220 |
| 0.11685 | 0.001735 |
| 0.12444 | 0.002468 |
| 0.13302 | 0.003511 |
| 0.14256 | 0.004993 |
| 0.15256 | 0.007102 |
| 0.16220 | 0.01010 |
| 0.17138 | 0.01437 |
| 0.18039 | 0.02044 |
| 0.18982 | 0.02907 |
| 0.20014 | 0.04135 |
| 0.21237 | 0.05881 |
| 0.22902 | 0.08365 |
| 0.25574 | 0.1190 |
| 0.30537 | 0.1692 |
| 0.42028 | 0.2407 |
| 0.56287 | 0.3424 |
| 0.71108 | 0.4870 |
| 0.86714 | 0.6927 |
| 1.0529 | 0.9852 |
| 1.2790 | 1.401 |
| 1.5661 | 1.993 |
| 1.8975 | 2.835 |

Acknowledgments

This work was sponsored by the Defense Advanced Research Projects Agency, under grant N66001-20-1-4028, and by the National Science Foundation under the award NSF-PHY-2028125. The content of the information does not necessarily reflect the position or the policy of the Government. No official endorsement should be inferred. Distribution statement A: approved for public release; distribution is unlimited.

References

- [1] Federal Communications Commission (FCC), https://licensing.fcc.gov/cgi-bin/ws.exe/prod/ib/forms/reports/swr031b.hts?q_set=V_SITE_ANTENNA_FREQ.file_numberC/File+Number/%3D/SATAMD2021 081800105&prepare=&column=V_SITE_ANTENNA_FREQ.file_numberC/File+Number [accessed 23 Dec. 2022].
- [2] Federal Communications Commission (FCC), https://licensing.fcc. gov/cgi-bin/ws.exe/prod/ib/forms/reports/swr031b.hts?q_set=V_SITE_

- ANTENNA_FREQ.file_numberC/File+Number/%3D/SATLOA202 1110400145&prepare=&column=V_SITE_ANTENNA_FREQ.file_numberC/File+Number [accessed 23 Dec. 2022].
- [3] Federal Communications Commission (FCC), https://licensing.fcc.gov/cgi-bin/ws.exe/prod/ib/forms/reports/swr031b.hts?q_set=V_SITE_ANTENNA_FREQ.file_numberC/File+Number/%3D/SATLOA2021 110400140&prepare=&column=V_SITE_ANTENNA_FREQ.file_numberC/File+Number [accessed 23 Dec. 2022].
- [4] Bowman, B., Tobiska, W. K., Marcos, F., Huang, C., Lin, C., and Burke, W., "A New Empirical Thermospheric Density Model JB2008 Using New Solar and Geomagnetic Indices," AIAA/AAS Astrodynamics Specialist Conference and Exhibit, AIAA Paper 2008-6348, Aug 2008
- [5] Lifson, M., Arnas, D., Linares, R., Ciencias, P. D., and Universitaria, C., "Low Earth Orbit Slotting: Implications for Orbit Design and Policy," 8th Annual Space Traffic Management Conference, International Academy of Astronautics Paper IAA-STM-22-02-06, Austin, TX, 2022, pp. 1–23.
- [6] Krag, H., Lemmens, S., and Letizia, F., "Space Traffic Management Through the Control of the Space Environment's Capacity," *1st IAA Conference on Space Situational Awareness (ICSSA)*, International Academy of Astronautics, 2017.
- [7] Rossi, A., Valsecchi, G., and Alessi, E., "The Criticality of Spacecraft Index," Advances in Space Research, Vol. 56, No. 3, 2015, pp. 449–460. https://doi.org/10.1016/j.asr.2015.02.027
- [8] Letizia, F., Colombo, C., Lewis, H., and Krag, H., "Extending the ECOB Space Debris Index with Fragmentation Risk Estimation," 7th European Conference on Space Debris, ESA Space Debris Office, Darmstadt, Germany, 2017.
- [9] Letizia, F., Lemmens, S., and Krag, H., "Environment Capacity as an Early Mission Design Driver," *Acta Astronautica*, Vol. 173, Aug. 2020, pp. 320–332.
- [10] Colombo, C., Trisolini, M., Muciaccia, A., Giudici, L., Gonzalo Gòmez, J., Frey, S., Del Campo, B., Letizia, F., and Lemmens, S., "Evaluation of the Share of the Space Capacity Share Used by a Mission," *International Astronautical Congress: IAC Proceedings*, International Astronautical Federation (IAF), Paris, France, 2022, pp. 1–13.
- [11] Liou, J.-C., Hall, D., Krisko, P., and Opiela, J., "LEGEND—A Three-Dimensional LEO-to-GEO Debris Evolutionary Model," *Advances in Space Research*, Vol. 34, No. 5, 2004, pp. 981–986. https://doi.org/10.1016/j.asr.2003.02.027
- [12] Lewis, H. G., Swinerd, G., Williams, N., and Gittins, G., "DAMAGE: A Dedicated GEO Debris Model Framework," *Proceedings of the Third European Conference on Space Debris*, edited by H. Sawaya-Lacoste, Vol. 1, ESA Publications Division, Noordwijk, The Netherlands, 2001, pp. 373–378.
- [13] Walker, R., Martin, C., Stokes, P., Wilkinson, J., and Klinkrad, H., "Analysis of the Effectiveness of Space Debris Mitigation Measures Using the DELTA Model," *Advances in Space Research*, Vol. 28, No. 9, 2001, pp. 1437–1445. https://doi.org/10.1016/S0273-1177(01)00445-8
- [14] Somma, G. L., "Adaptive Remediation of the Space Debris Environment Using Feedback Control," Ph.D. Thesis, Univ. of Southampton, Southampton, England, U.K., 2019, https://eprints.soton.ac.uk/403265/.
- [15] Kessler, D. J., and Cour-Palais, B. G., "Collision Frequency of Artificial Satellites: The Creation of a Debris Belt," *Journal of Geophysical Research: Space Physics*, Vol. 83, No. A6, 1978, pp. 2637–2646. https://doi.org/10.1029/JA083iA06p02637
- [16] Kessler, D. J., and Anz-Meador, P. D., "Critical Number of Spacecraft in Low Earth Orbit: Using Satellite Fragmentation Data to Evaluate the Stability of the Orbital Debris Environment," *European Space Agency*, (Special Publication) ESA SP, Vol. 1, No. 473, 2001, pp. 265–272. https://doi.org/2011ESASP.473..265K
- [17] Kessler, D. J., Johnson, N. L., Liou, J., and Matney, M., "The Kessler Syndrome: Implications to Future Space Operations," *Advances in the*

- Astronautical Sciences, Vol. 137, No. 8, 2010, p. 1016; also AAS Paper 10-1016, 2010.
- [18] Talent, D. L., "Analytic Model for Orbital Debris Environmental Management," *Journal of Spacecraft and Rockets*, Vol. 29, No. 4, 1992, pp. 508–513.
- [19] Somma, G. L., Colombo, C., and Lewis, H., "A Statistical LEO Model to Investigate Adaptable Debris Control Strategies," 7th European Conference on Space Debris, ESA Space Debris Office, Darmstadt, Germany, 2017, pp. 1–12.
- [20] Trozzi, V., Colombo, C., and Trisolini, M., "Analysis of Possible Definitions of the Space Environment Capacity to Pursue Long-Term Sustainability of Space Activities," 72nd International Astronautical Congress (IAC 2021), International Astronautical Federation (IAF), Paris, France, 2021, pp. 1–14.
- [21] D'Ambrosio, A., Lifson, M., and Linares, R., "The Capacity of Low Earth Orbit Computed Using Source-Sink Modeling," June 2022. https://doi.org/10.48550/ARXIV.2206.05345
- [22] Letizia, F., Virgili, B. B., and Lemmens, S., "Assessment of Orbital Capacity Thresholds Through Long-Term Simulations of the Debris Environment," Advances in Space Research (in press).
- [23] Iridium, OneWeb, SpaceX, Satellite Orbital Safety Best Practices, https://assets.oneweb.net/s3fs-public/2022-09/Satellite%20Orbital% 20Safety%20Best%20Practices.pdf [accessed 23 Dec. 2022].
- [24] White, A. E., and Lewis, H. G., "An Adaptive Strategy for Active Debris Removal," *Advances in Space Research*, Vol. 53, No. 8, 2014, pp. 1195–1206.
- [25] Krisko, P., "Proper Implementation of the 1998 NASA Breakup Model," Orbital Debris Quarterly News, Vol. 15, No. 4, 2011, pp. 1–10.
- [26] Tobiska, W. K., Bowman, B. R., and Bouwer, S. D., "Solar and Geomagnetic Indices for Thermospheric Density Models," COSPAR International Reference Atmosphere, edited by D. Rees, and W. K. Tobiska, Chap. 4, https://spacewx.com/wp-content/uploads/2021/03/Ch4_solar_geomag_indices.pdf [accessed 23 Dec. 2022].
- [27] Vallado, D. A., Fundamentals of Astrodynamics and Applications, 4th ed., edited byJ. Wertz, Microcosm Press/Springer, Hawthorne, CA, 2013, p. 567, Chap. 8.
- [28] Choi, E.-J., Cho, S., Jo, J. H., Park, J.-H., Chung, T., Park, J., Jeon, H., Yun, A., and Lee, Y., "Performance Analysis of Sensor Systems for Space Situational Awareness," *Journal of Astronomy and Space Sciences*, Vol. 34, No. 4, 2017, pp. 303–314. https://doi.org/10.5140/JASS.2017.34.4.303
- [29] Murray, J., Blackwell, C., Gaynor, J., and Kennedy, T., "Haystack Ultra-Wideband Satellite Imaging Radar Measurements of the Orbital Debris Environment: 2014-2017," NASA, Lyndon B. Johnson Space Center Houston, Texas, 2019, https://ntrs.nasa.gov/api/citations/201900287 19/downloads/20190028719.pdf [accessed 15 June 2022].
- [30] Li, H.-J., and Kiang, Y.-W., "Radar and Inverse Scattering," The Electrical Engineering Handbook, Academic Press, New York, 2005, pp. 671– 600
- [31] JASON Program Office, "The Impact of Large Constellations of Satellites," 2020, https://www.nsf.gov/news/special_reports/jasonreport constellations/ [1 Feb. 2022].
- [32] Somma, G. L., Lewis, H. G., and Colombo, C., "Sensitivity Analysis of Launch Activities in Low Earth Orbit," *Acta Astronautica*, Vol. 158, May 2019, pp. 129–139. https://doi.org/10.1016/j.actaastro.2018.05.043
- [33] MASTER-8.0.3, https://sdup.esoc.esa.int/master/downloads [accessed 15 July 2022].
- [34] Enhancement of S/C Fragmentation and Environment Evolution Models (Final Report), https://sdup.esoc.esa.int/master/downloads/documentation/ 8.0.3/MASTER-8-Final-Report.pdf [accessed 23 Dec. 2022].

C. N. McGrath Associate Editor